Article

Cell Reports

Re-education of Tumor-Associated Macrophages by CXCR2 Blockade Drives Senescence and Tumor Inhibition in Advanced Prostate Cancer

Graphical Abstract

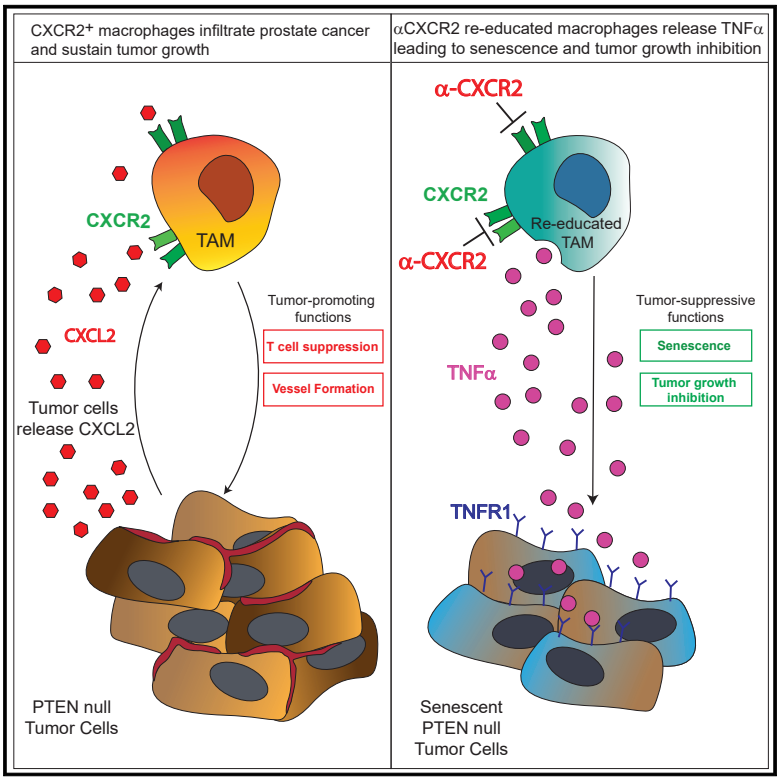

Highlights

- CXCR2 blockade drives re-education of tumor-associated macrophages (TAMs)
- Infusion of CXCR2-KO monocytes in tumor-bearing mice blocks tumor progression
- PTEN deletion sensitizes tumor cells to TNF-α-induced senescence and growth arrest

Authors

Diletta Di Mitri, Michela Mirenda, Jelena Vasilevska, ..., Simon Barry, Johann De Bono, Andrea Alimonti

Correspondence

andrea.alimonti@ior.usi.ch

In Brief

Di Mitri et al. show that CXCR2 blockade in prostate cancer triggers TAMs re-education, leading to tumor inhibition. CXCR2-KO monocytes infused in $Pten^{pc-/-}$; $Trp53^{pc-/-}$ tumor-bearing mice differentiate into TNFα-releasing pro-inflammatory macrophages that induce senescence in tumor cells. PTEN-null tumors display higher sensitivity to TNF-α-induced senescence because of TNFR1 upregulation.

Di Mitri et al., 2019, Cell Reports *28*, 2156–2168
August 20, 2019
https://doi.org/10.1016/j.celrep.2019.07.068

CellPress

OPEN ACCESS
CellPress

Cell Reports
Article

Re-education of Tumor-Associated Macrophages by CXCR2 Blockade Drives Senescence and Tumor Inhibition in Advanced Prostate Cancer

Diletta Di Mitri,[1,18] Michela Mirenda,[2,18] Jelena Vasilevska,[2,18] Arianna Calcinotto,[2] Nicolas Delaleu,[3,4,5] Ajinkya Revandkar,[2] Veronica Gil,[6] Gunther Boysen,[6] Marco Losa,[2] Simone Mosole,[2] Emiliano Pasquini,[2] Rocco D'Antuono,[7] Michela Masetti,[1] Elena Zagato,[2] Giovanna Chiorino,[8] Paola Ostano,[8] Andrea Rinaldi,[2] Letizia Gnetti,[9] Mariona Graupera,[10,11,12] Ana Raquel Martins Figueiredo Fonseca,[10,11,12] Ricardo Pereira Mestre,[17] David Waugh,[13] Simon Barry,[14] Johann De Bono,[6] and Andrea Alimonti[2,15,16,17,19,*]

[1]Istituto Clinico Humanitas, Istituto di Ricovero e Cura a Carattere Scientifico (IRCCS), Via A. Manzoni 113, 20089 Rozzano, Milan, Italy
[2]Institute of Oncology Research (IOR), 6500 Bellinzona, Switzerland
[3]Broegelmann Research Laboratory, Department of Clinical Science, University of Bergen, 5021 Bergen, Norway
[4]Swiss Institute of Bioinformatics, Lausanne, Switzerland
[5]2C SysBioMed, 6646 Contra, Switzerland
[6]The Institute of Cancer Research and The Royal Marsden NHS Foundation Trust, London, UK
[7]Institute for Research in Biomedicine (IRB), 6500 Bellinzona, Switzerland
[8]Cancer Genomics Lab, Fondazione Edo ed Elvo Tempia, Via Malta, 3, 13900 Biella, Italy
[9]Pathology Unit, University Hospital of Parma, 43126 Parma, Italy
[10]Vascular Signalling Laboratory, Institut d'Investigació Biomèdica de Bellvitge (IDIBELL), Barcelona, Spain
[11]Program Against Cancer Therapeutic Resistance (ProCURE), Barcelona, Spain
[12]CIBERONC, Madrid, Spain
[13]Movember Centre of Excellence, Centre for Cancer Research and Cell Biology, Queen's University Belfast, Belfast, UK
[14]IMED Oncology AstraZeneca, Li KaShing Centre, Cambridge, UK
[15]Faculty of Medicine, Università della Svizzera Italiana, 1011 Lugano, Switzerland
[16]Department of Medicine, University of Padua, 35131 Padua, Italy
[17]Medical Oncology, Oncology Institute of Southern Switzerland, 6500 Bellinzona, Switzerland
[18]These authors contributed equally
[19]Lead Contact
*Correspondence: andrea.alimonti@ior.usi.ch
https://doi.org/10.1016/j.celrep.2019.07.068

SUMMARY

Tumor-associated macrophages (TAMs) represent a major component of the tumor microenvironment supporting tumorigenesis. TAMs re-education has been proposed as a strategy to promote tumor inhibition. However, whether this approach may work in prostate cancer is unknown. Here we find that *Pten*-null prostate tumors are strongly infiltrated by TAMs expressing C-X-C chemokine receptor type 2 (CXCR2), and activation of this receptor through CXCL2 polarizes macrophages toward an anti-inflammatory phenotype. Notably, pharmacological blockade of CXCR2 receptor by a selective antagonist promoted the re-education of TAMs toward a pro-inflammatory phenotype. Strikingly, CXCR2 knockout monocytes infused in $Pten^{pc-/-}$; $Trp53^{pc-/-}$ mice differentiated in tumor necrosis factor alpha (TNF-α)-releasing pro-inflammatory macrophages, leading to senescence and tumor inhibition. Mechanistically, *PTEN*-deficient tumor cells are vulnerable to TNF-α-induced senescence, because of an increase of *TNFR1*. Our results identify TAMs as targets in prostate cancer and describe a therapeutic strategy based on CXCR2 blockade to harness anti-tumorigenic potential of macrophages against this disease.

INTRODUCTION

Immunotherapy based on reactivation of T cells in the tumor microenvironment is emerging as an effective strategy to treat cancer. However, in several tumors, such as in prostate cancer, T cells constitute only a minor component of the tumor immune response compared with tumor-associated macrophages (TAMs), the most abundant noncancerous cell type (Nava Rodrigues et al., 2018). Macrophages are a plastic immune population that can be polarized *in vitro* in anti-inflammatory subsets by cytokines, such as IL-4 and IL-13, or into pro-inflammatory immune cells by IFNγ. However, these extreme macrophage phenotypes do not fully recapitulate the plasticity of TAMs *in vivo*, where macrophages are polarized to different and more complex phenotypes. Indeed cancer cells can influence TAMs polarization by releasing cytokines, glucocorticoids, extracellular vesicles, and extracellular matrix components that give rise to a large spectrum of pro-tumoral macrophages (Cassetta et al., 2019). In prostate cancer, TAMs and other myeloid subsets constitute up

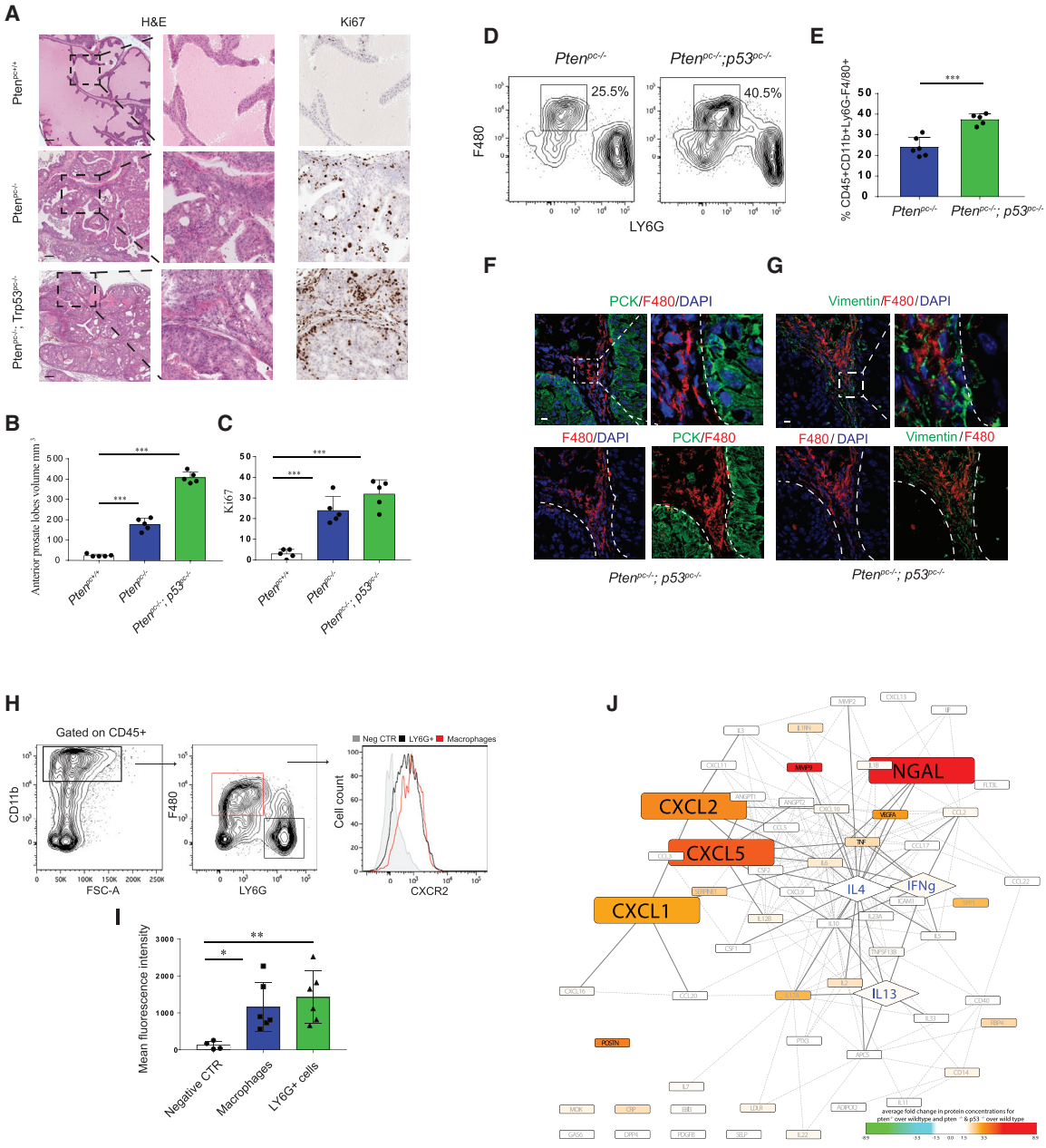

Figure 1. Tumor-Associated Macrophages (TAMs) Infiltrate Prostate Cancer and Express CXCR2

(A) Representative images of H&E and Ki-67 IHC staining. Original magnification, 20×. Scale bar: 100 μm.

(B and C) Anterior prostate lobe volume (mm^3) (B) (see STAR Methods) and Ki-67 quantification (C) in 12-week-old *Pten*$^{pc+/+}$, *Pten*$^{pc-/-}$; *Trp53*$^{pc+/+}$ (*Pten*$^{pc-/-}$), and *Pten*$^{pc-/-}$; *Trp53*$^{pc-/-}$mice (n = 5 mice per group).

(D and E) Representative FACS plots of immunophenotyping (D) and quantification (E) of tumor-infiltrating $CD11b^+Ly6G^-F4/80^+$ macrophages in 12-week-old *Pten*$^{pc-/-}$ and *Pten*$^{pc-/-}$; *Trp53*$^{pc-/-}$ mice. Events are gated on $CD45^+CD11b^+$ cells (n = 5 per group).

(F) Representative confocal immunofluorescence (IF) images and quantification showing the localization of $F4/80^+$ (red) macrophages in *Pten*$^{pc-/-}$; *Trp53*$^{pc-/-}$prostatic tumors. Prostatic epithelial tissue is stained with αPan-Cytokeratin antibody (PCK; green). Cells were counterstained with the nuclear marker DAPI (blue). Scale bar, 10 μm (n = 3 mice per group).

(G) Representative confocal immunofluorescence images of $F4/80^+$ (red) tumor-infiltrating macrophages in *Pten*$^{pc-/-}$; *Trp53*$^{pc-/-}$prostatic tumors. Stromal cells are stained with anti-vimentin antibody (vimentin; green). Cells were counterstained with the nuclear marker DAPI (blue). Scale bar, 10 μm (n = 3 mice per group).

(H and I) Representative FACS analysis (H) and quantification (I) of the mean fluorescence index (MFI) per cell of CXCR2 expression on TAMs and neutrophils in *Pten*$^{pc-/-}$; *Trp53*$^{pc-/-}$ prostatic tumors (n = 6 mice). Mean fluorescence intensity was measured on $CD11b^+CD45^+F480^+Ly6G^-$ TAMs and $CD11b^+CD45^+F480^-LY6G^+$ neutrophils.

(legend continued on next page)

to 70% of tumor immune subsets (Calcinotto et al., 2018) and are known to influence tumor growth by controlling adaptive immunity, angiogenesis, tumor cell proliferation, and metastasis formation, thus playing a fundamental role in cancer initiation, progression, and resistance to treatment (Baer et al., 2016; Bingle et al., 2002; Guerriero et al., 2017; Kaneda et al., 2016; Mantovani et al., 2006; Qian and Pollard, 2010). As a consequence, TAMs provide an ideal target for therapy in cancer patients. Although strategies to deplete TAMs have been extensively investigated in the clinical setting in different cancer types (Guerriero et al., 2017; Pienta et al., 2013; Ries et al., 2014), the reported overall benefit for cancer patients has been negligible (Mantovani et al., 2017). The limited success of this approach has been ascribed to the plasticity of TAMs. In the tumor microenvironment, TAMs work as either anti- or pro-tumoral components, and the removal of anti-tumoral TAMs blunts the efficacy of TAM-depleting therapies (Mantovani et al., 2017). Exploiting the tumor-homing ability of TAMs and their plasticity by treatments that can re-educate TAMs toward a pro-inflammatory, anti-tumorigenic functional status may lead to more effective and long-lasting responses in cancer patients. In this regard, re-education of TAMs toward a pro-inflammatory, anti-tumorigenic functional status has been recently proposed as a potential therapeutic approach to treat different types of cancer, including prostate cancer (Guerriero et al., 2017; Hagemann et al., 2009; Pyonteck et al., 2013; Salvagno et al., 2019). In prostate cancer the frequency and activation state of infiltrating macrophages have been associated with disease progression and therapy resistance (Escamilla et al., 2015; Lanciotti et al., 2014; Nonomura et al., 2010). Nevertheless, current knowledge on the interplay between macrophages and prostate cancer is still limited, and further investigation is required. Moreover, it is unknown whether compounds that re-educate TAMs in order to promote their tumor-suppressive function may suppress the proliferation of aggressive prostate cancer. In the present paper we identify the macrophage receptor CXCR2 and CXCR2 signaling as major drivers of TAMs polarization in prostate tumors, and we propose a therapeutic strategy based on blockade of the CXCL-CXCR2 pathway or infusion of CXCR2 knockout (KO) monocytes to harness the anti-tumorigenic potential of macrophages against prostate cancer.

RESULTS

CXCR2-Expressing TAMs Infiltrate Prostate Cancer

To better understand the mechanism by which prostate tumor cells affect the functional polarization of TAMs, we compared two *Pten*-null prostate conditional (pc−/−) mouse models, in which *Trp53* expression in prostate is respectively maintained or depleted (Alimonti et al., 2010; Chen et al., 2005). These two models recapitulate pathological and molecular features of human prostate cancer at different stages of progression, with $Pten^{pc-/-}$; $Trp53^{pc-/-}$ tumors more invasive compared with $Pten^{pc-/-}$; $Trp53^{pc+/+}$ ($Pten^{pc-/-}$) (Figures 1A–1C). Flow cytometry analyses showed that both $Pten^{pc-/-}$ and $Pten^{pc-/-}$; $Trp53^{pc-/-}$ tumors are strongly infiltrated by $CD45^+$ $CD11b^+LY6G^-F4/80^+$ macrophages and that TAMs frequency slightly increases with tumor progression (Figures 1D and 1E; see Figure S1A for the gating strategy). Immunofluorescence staining confirmed the prominent infiltration of TAMs in both $Pten^{pc-/-}$ and $Pten^{pc-/-}$; $Trp53^{pc-/-}$ tumors (Figure 1F; Figure S1B). Importantly, TAMs are localized mainly in the $vimentin^+$ surrounding stroma of prostatic tumors (Figures 1G and S1C). A prominent increase of $CD68^+$ TAMs was also detected in human prostate cancers compared with PIN sections (Figures S1D–S1F), thus confirming previous evidence (Lanciotti et al., 2014). Strikingly, we found that the majority of tumor-infiltrating $CD45^+CD11b^+LY6G^-F4/80^+$ macrophages expressed the CXCR2 receptor, at levels comparable with the $CD45^+$ $CD11b^+LY6G^+F4/80^-$ granulocytic subset, as shown by flow cytometry performed on single-cell suspension obtained from $Pten^{pc-/-}$; $Trp53^{pc-/-}$ tumors (Figures 1H and 1I). Accordingly, protein profiling performed through a cytokine array revealed a significant upregulation of the CXCL1, CXCL2, and CXCL5, three ligands of the C-X-C motif chemokine receptor 2 (CXCR2), in both $Pten^{pc-/-}$ and $Pten^{pc-/-}$; $Trp53^{pc-/-}$ tumors (Figure 1J). Analysis of public available gene expression data confirmed the upregulation of ELR+CXCL chemokines in *Pten*-null tumors (Figure S1G).

CXCR2 Engagement Tilts Macrophages Polarization toward a Pro-tumorigenic Functional State *In Vitro*

To assess the role of the CXCL-CXCR2 axis in the polarization of macrophages, we isolated and differentiated bone marrow-derived macrophages (BMDMs) from C57BL/6 mice and exposed them to CXCL2 recombinant protein, the most upregulated CXCL chemokine in our tumor models, in a polarization assay *in vitro*. Gene expression analysis performed on these cells revealed a marked upregulation of arginase and CD206, genes that are generally associated with anti-inflammatory macrophages, in CXCL2-educated cells, while pro-inflammatory genes such as tumor necrosis alpha (TNF-α) and IL-12 were not significantly enriched or were even decreased in these samples (Figure 2A). Subsequently we applied an unbiased gene expression analysis to CXCL2-stimulated macrophages. Pro-inflammatory IFNγ/LPS-polarized macrophages and anti-inflammatory and pro-angiogenic IL-4/IL-13 alternatively activated macrophages were used as controls (Martinez and Gordon, 2014). Interestingly, analysis of pivotal gene sets (GSs) revealed a significant overlap (83.6%) in the transcriptional landscape of

(J) Graph showing analysis of the protein expression profiling from epithelia isolated from $Pten^{pc-/-}$ and $Pten^{pc-/-}$; $Trp53^{pc-/-}$ tumors. One hundred ten proteins were analyzed by mean of the XL mouse protein array kit (R&D). All proteins included in our panel were assessed for their possible involvement in macrophage polarization by applying text-mining algorithms (Agilent Literature Search 3.1.1, in Cytoscape 3.1.1) for a minimum of 40 papers per protein. A node's color represents mean fold change for $Pten^{pc-/-}$ versus wild-type and $Pten^{pc-/-}$; $Trp53^{pc-/-}$ versus wild-type. Genes consistently yielding a >2-fold increase for both comparisons and showing significant matching trends for their gene expression profiles (Figure S1E) are magnified. Classical and alternatively activating polarizers are annotated with blue as font color and displayed as diamonds.
Error bars are mean ± SEM. ***$p < 0.001$.

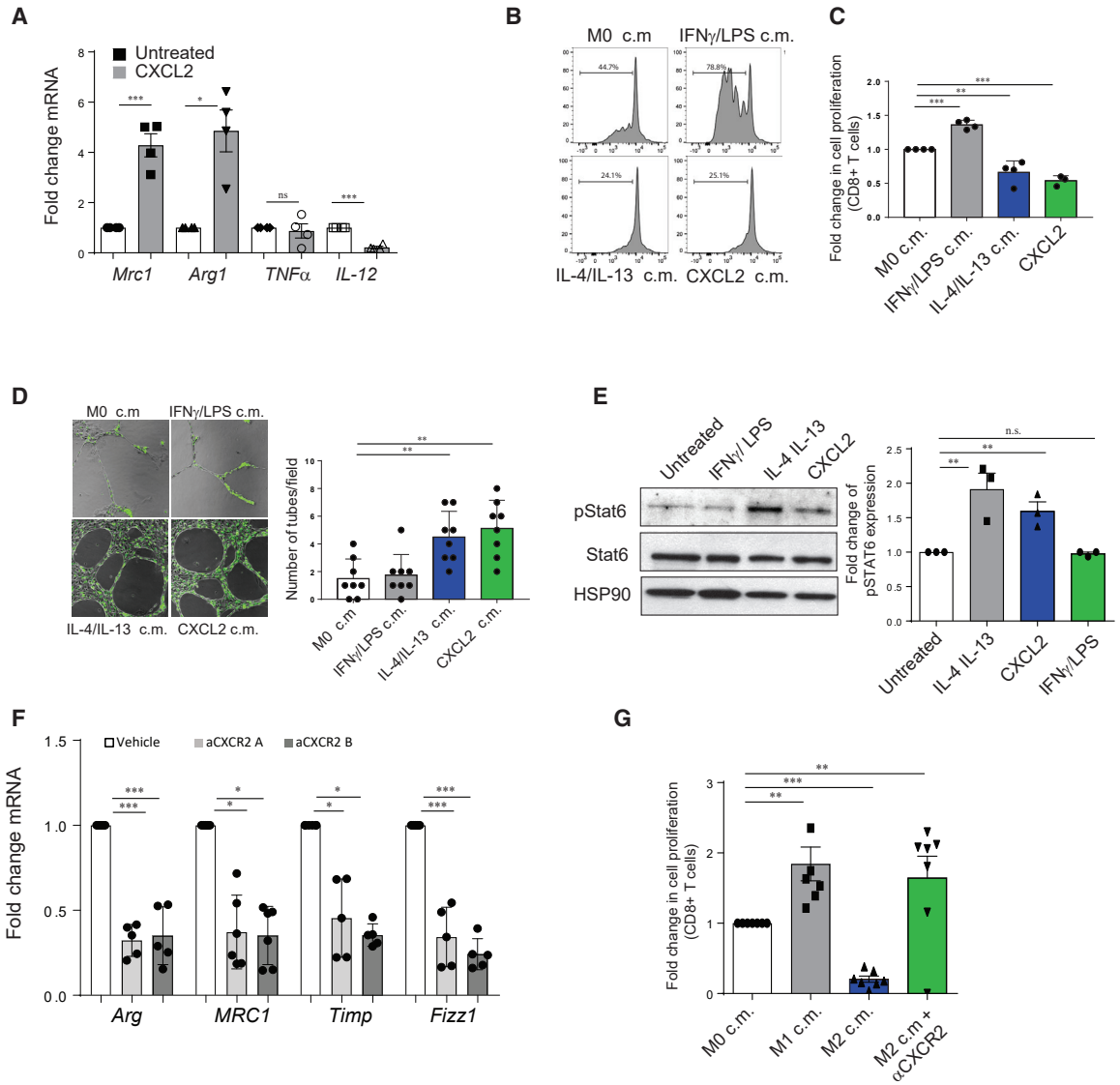

Figure 2. CXCL2 Administration Induces a Suppressive and Pro-angiogenic Functional State in Macrophages *In Vitro*

(A) RT-qPCR gene expression analysis of BMDMs polarized *in vitro* upon administration of CXCL2 recombinant protein (n = 4).

(B and C) FACS analysis (B) and quantification (C) showing a carboxyfluorescein succinimidyl ester (CFSE) proliferation assays performed on isolated splenocytes exposed to macrophage-derived conditioned media (n = 3). Plots show the percentage of $CD8^{+}CFSE^{-}$ proliferating cells. Macrophages were polarized in presence of stimuli for 48 h, then media was washed out and replaced. Conditioned media for the experiment was collected after 24 h.

(D) Representative pictures of immunofluorescence staining (left panel) and quantification (right panel) showing a tube formation assays performed on CECs (cardiac endothelial murine cells) exposed to macrophage-derived conditioned media (n = 3). Macrophages were polarized in presence of stimuli for 48 h, then media was washed out and replaced. Conditioned media for the experiment was collected after 24 h.

(E) Western blot analysis (left panel) showing the levels of total Stat6, phosphorylated Stat6, and HSP90 in IL-4/IL-13 and CXCL2-polarized macrophages. The bar graph (right panel) shows the levels of pStat6 expression. The levels of pStat6 expression were normalized for the levels of total Stat6 in each sample.

(F) RT-qPCR gene expression analysis of alternative macrophages prototypic markers on macrophages polarized *in vitro* in absence or presence of αCXCR2 1 (1 μM, SB265610) and αCXCR2 (1 μM, SB225002) (n = 5).

(G) FACS analysis and quantification of a CFSE proliferation assay on isolated splenocytes exposed to macrophage-derived conditioned media in absence or presence of SB265610. Quantification is based on the frequency of $CD8^{+}CFSE^{-}$ proliferating cells (n = 5).

Error bars are mean ± SEM. *p < 0.05, **p < 0.01, and ***p < 0.001.

CXCL2 and IL-4/IL-13-stimulated macrophages (Figure S2A). In addition, profiling of 110 proteins performed by a proteome profiler cytokine array showed a substantial correspondence in the type of proteins secreted by the two groups (Figure S2B). To therefore test the functional status of CXCL2-stimulated macrophages, we exposed macrophages to CXCL2 *in vitro* for 24 h, we washed the cells to replace normal DMEM, and after 48 h we collected the conditioned media (c.m.). Strikingly, c.m. from

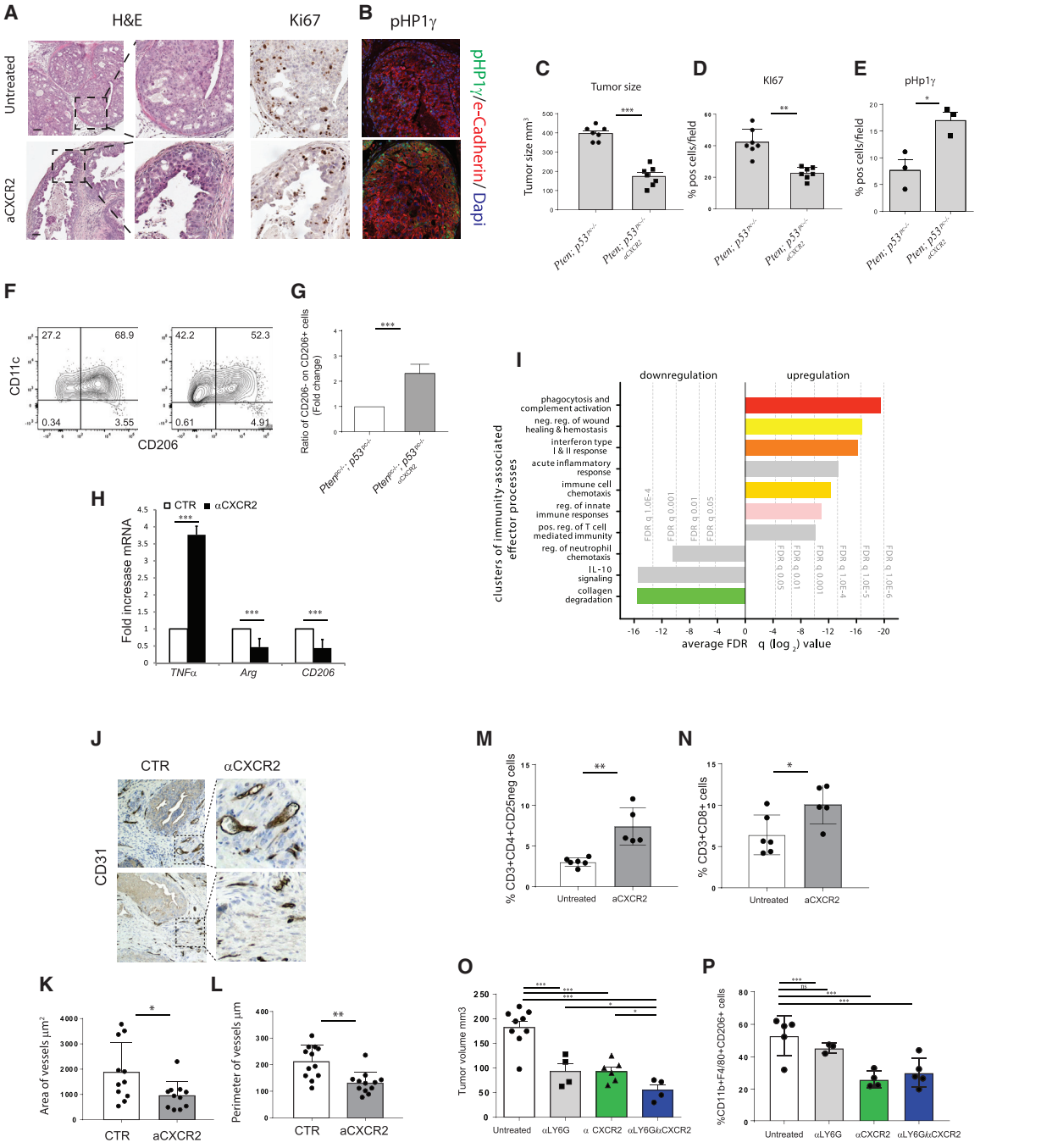

Figure 3. αCXCR2-Mediated TAMs Reprogramming Induces Tumor Regression and Modulates T Cell Response and Vessel Size.

Mice were treated with αCXCR2 (AZD5069 100 mg/kg) or vehicle, starting at the age of tumor formation (8 weeks), for 3 weeks.

(A) Representative images of H&E (right panel) and Ki-67 IHC staining (right panel). Original magnification, 20×; scale bar, 50 μm.

(B) pHp1γ IF staining. Original magnification, 20×; scale bar, 25 μm.

(C) Volume of anterior prostate lobes (see STAR Methods); n = 7.

(D) and E) Ki-67 (D) and pHp1γ quantification (E) in *Pten*$^{pc-/-}$; *p53*$^{pc-/-}$ prostatic tumors upon αCXCR2 treatment (n = 7 and n = 3, respectively).

(F and G) Representative immunophenotyping plot (F) and quantification (G) of CD11c^{+}CD206^{-} pro-inflammatory and CD11c$^{+/-}$CD206^{+} tumor-promoting macrophages (Mazzieri et al., 2011) infiltrating the tumor upon administration of αCXCR2. Events are gated on CD45^{+}CD11b^{+}F4/80^{+} cells (n = 5 mice per group).

(H) RT-qPCR gene expression analysis on CD45^{+}/F4/80^{+} macrophages sorted from tumors (n = 4).

(I) Unbiased systematic analyses of coordinated alterations following gene expression profiling in TAMs isolated from the prostate of untreated and αCXCR2-treated mice (n = 3 per group). Graph shows significantly altered clusters of immunity-associated effector processes. Bars represent the average $\log_2$FDRq values of the gene sets included in each cluster.

(legend continued on next page)

CXCL2-polarized macrophages reduced $CD8^+$ proliferation in a suppression assay (Figures 2B and 2C; see Figure S2C for the gating strategy). These findings were further confirmed on $CD8^+$ T cells sorted from murine lymph nodes and $CD8^+$ cells gated from murine peripheral blood (Figures S2D and S2E). Further functional analysis showed that CXCL2-stimulated macrophages promote the formation of capillary-like structures (tubes) from endothelial murine cells (Figure 2D). Results reported above indicate that CXCL2 promotes macrophage differentiation toward an alternative activation state. In line with this evidence, we detected increased protein levels of pSTAT6 in both canonical (IL-4/IL-13) and CXCL2-polarized macrophages (Takeda et al., 1996) (Figure 2E). Therefore, we checked whether CXCR2 inhibition could affect IL-4/IL-13 polarization. Our flow cytometry analysis showed an increase in the levels of CXCR2 upon IL-4/IL-13 activation of BMDMs (Figure S2F). Finally, treatment with two different CXCR2 antagonists (αCXCR2) reverted the macrophage polarization toward the anti-inflammatory state driven by IL-4 and IL-13, as shown by the decrease expression of prototypic genes and a $CD8^+$T cells suppression assay *in vitro* (Figures 2F and 2G).

Pharmacological Disruption of the CXCL2-CXCR2 Pathway Triggers Tumor Inhibition and TAMs Re-education

Altogether, the findings reported above support the importance of the CXCL-CXCR2 axis in the induction of an anti-inflammatory functional state in macrophages. To validate this hypothesis *in vivo*, we took advantage of the $Pten^{pc-/-}$; $Trp53^{pc-/-}$ mouse model, which develops highly aggressive prostate cancers compared with $Pten^{pc-/-}$ mice. Therefore we treated $Pten^{pc-/-}$; $Trp53^{pc-/-}$ mice with AZD5069, a potent and selective antagonist of CXCR2 under clinical development (Steele et al., 2016) (ClinicalTrials.gov: NCT03177187). Gross macroscopic and histological analyses of $Pten^{pc-/-}$; $Trp53^{pc-/-}$ tumors treated with-AZD5069 showed a strong suppression of tumor size and presence of normalized prostate areas compared with the untreated control (Figure 3A). Remarkably, AZD5069 treatment induced a strong reduction of Ki-67 staining and upregulation of senescence as detected by increased levels of pHP1γ and p16 (Figures 3A–3E; Figures S3A and S3B). Western blot analysis showed increased levels of GATA4, an additional marker of senescence (Kang et al., 2015), in tumors treated with AZD5069 (Figures S3C and S3D). Importantly, αCXCR2 treatment *in vitro* did not affect prostate epithelial cell proliferation and did not drive senescence per se, demonstrating that the effect of αCXCR2 is indirect (Figure S3E). To evaluate the effect of the CXCR2 blockade on infiltrating macrophages, we investigated the immune infiltrate of tumors by fluorescence-activated cell sorting (FACS) analysis. Our results showed a reduction of $F4/80^+CD11c^{+/-}CD206^+$ cells, previously described as pro-angiogenic macrophages in different tumors, in favor of $F4/80^+CD11c^+CD206^-$ pro-inflammatory TAMs (Figures 3F and 3G) (Mazzieri et al., 2011). Accordingly, RT-qPCR analysis showed a significant increase in TNFα mRNA levels (generally associated with pro-inflammatory TAMs) and downregulation of arginase and CD206 levels (generally associated with anti-inflammatory TAMs) in TAMs isolated from mice treated with αCXCR2 (Figure 3H) (Mosser and Edwards, 2008; Rath et al., 2014). These findings were also validated in an isogenic TRAMP-C1 cell line in which *Pten* was deleted by using a Crispr-Cas9 system thereby generating the *Pten*-null; *Trp53*-inactivated prostate epithelial cells ($Pten^{-/-}$-TRAMP-C1) (Figure S4A). $Pten^{-/-}$-TRAMP-C1 cells were subcutaneously injected *in vivo*, and mice were treated with AZD5069. As observed in the transgenic model, AZD5069 treatment resulted in a reduction in tumor size (Figure S4B) and in the re-education of TAMs (Figure S4C). Of note, re-educated macrophages expressed a higher amount of TNFα upon αCXCR2 treatment (Figure S4D). $Pten^{-/-}$-TRAMP-C1 allografts also showed an increased senescence induction upon aCXCR2 treatment, as demonstrated by the upregulation of p16, pH2AX foci, and GATA4 expression, three well-characterized markers of senescence (Figures S4E–S4H) (Kang et al., 2015).

Notably, treatment of $Pten^{pc-/-}$; $Trp53^{pc-/-}$ mice with AZD5069 strongly affected the gene expression profile of $CD45^+CD11b^+LY6G^-F4/80^+$ sorted TAMs. Indeed, unbiased systematic analyses of coordinated alterations following gene expression profiling in sorted TAMs, resulted in the over- and under-representation of 312 GSs in AZD5069 treated mice compared with untreated animals (Figure 3I). Among the gene processes that were modulated in sorted macrophages upon AZD5069 administration, we detected a significant activation of pro-inflammatory immunity-associated effector processes and depletion of processes related to pro-tumorigenic functions, IL-10 signaling, and collagen degradation (Figures S4I and S4J). This evidence indicates a reprogramming of TAMs from a pro-tumorigenic to a pro-inflammatory phenotype in αCXCR2-treated mice. In accordance with the results of the GS analysis and our *in vitro* evidence, AZD5069 treatment resulted in a strong inhibition of vessel formation (Figures 3J–3L) in the treated tumors. Furthermore, a comprehensive analysis of the tumor immune infiltrate upon CXCR2 blockade revealed that the frequency of $CD45^+CD11b^+LY6G^-F4/80^+$macrophages was not affected by the treatment (Figure S5A). Importantly, we observed an increased infiltration of $CD4^+$ and $CD8^+$ T cells in the treated

(J) Representative images of CD31 IHC staining on anterior lobe prostate of $Pten^{pc-/-}$; $Trp53^{pc-/-}$mice upon αCXCR2 treatment. Original magnification 20×.
(K and L) Quantification of area (K) and perimeter (L) of vessels in the tumor area (n = 3).
(M and N) Quantification of the frequency of infiltrating $CD4^+CD25^-$ (M) and $CD8^+$ T cells (N) in prostatic tumors before and after αCXCR2 treatment. Events are gated on $CD45^+$ cells (n = 5 mice per group).
(O) Volume of anterior prostate lobes (see STAR Methods) at the end of the treatments.
(P) Quantification of $CD45^+CD11b^+F4/80^+CD206^+$ anti-inflammatory macrophages infiltrating the tumor upon treatments. $Pten^{pc-/-}$; $Trp53^{pc-/-}$mice were treated with αCXCR2 (AZD5069 100 mg/kg), 1A8 (αLy6G antibody), or αCXCR2/1A8 for 3 weeks, starting at the age of tumor formation (8 weeks). Events are gated on $CD45^+CD11b^+$ cells (n = 4 mice per group).
Error bars are mean ± SEM. *p < 0.05, *p < 0.01, and ***p < 0.001.

tumors (Figures 3M and 3N; Figures S5A and S5B for the gating strategy), associated with activation of the $CD8^+$ subset, as indicated by granzyme B staining (Figures S5C and S5D). Further analysis of the $CD3^+$ infiltrate showed that the frequency of $CD4^+$ regulatory cells was not significantly affected by the CXCR2 blockade (Figures S5E and S5F).

As an additional investigation of TAMs reprogramming upon CXCR2 blockade, we performed *in vitro* assays with tumor-conditioned macrophages exposed to αCXCR2. Our assays showed that the phagocytic activity of macrophages was increased upon CXCR2 blockade, thus confirming the *ex vivo* gene expression data (Figures S5G and S5H). Additionally, tumor-conditioned macrophages exposed to αCXCR2 were able to induce a senescence response in target tumor cells (Figures S5I and S5J). We next investigated whether the infiltration of $CD11b^+F480^-Ly6G^+$myeloid cells was affected by αCXCR2 treatment. We found that CXCR2 blockade only slightly affected the recruitment of $CD11b+F480^{neg}$ $Ly6G^+$ cells in $Pten^{pc-/-}$; $Trp53^{pc-/-}$ tumors (Figures S6A and S6B), probably because of the presence of additional cytokines capable of recruiting these immune cells as previously reported by others (Patnaik et al., 2017). To further explore the role of $LY6G^+$ cells in our settings, we performed a pre-clinical trial combining aCXCR2 with a neutralizing antibody for LY6G. Our results indicated that CXCR2 blockade resulted in a strong tumor inhibition and macrophage reprogramming also in absence of $Ly6G^+$ cells, as shown by flow cytometry and immunohistochemical analyses. Moreover, combination of aCXCR2 and anti-LY6G increased tumor growth inhibition compared with the single treatments (Figures 3O and 3P; Figures S6C and S6D). Altogether, these findings demonstrate that inhibition of the CXCR2 receptor in $Pten^{pc-/-}$; $Trp53^{pc-/-}$ tumors *in vivo* results in the re-education of tumor-infiltrating macrophages toward a pro-inflammatory and anti-tumorigenic functional state and in a strong activation of a p53-independent cellular senescence response.

Infusion of CXCR2-KO Monocytes Drives Tumor Inhibition and Senescence Induction in $Pten^{pc-/-}$; $p53^{pc-/-}$ Tumor-Bearing Mice

Autologous infusion of human IFNγ-activated monocytes was attempted in the past to treat cancer-bearing patients. However, such infusions resulted in poor clinical response, because monocytes reaching the tumors were polarized mainly toward alternatively activated TAMs. Indeed, high TNFα levels were never detected in the serum of treated patients even after several infusions (Lopez et al., 1992, 1994; Stevenson et al., 1988). We therefore hypothesized that infusion of CXCR2-KO monocytes in tumor-bearing mice could overcome this problem. To test our hypothesis, we infused CXCR2 wild-type (WT) and CXCR2-KO bone marrow-derived monocytes in $Pten^{pc-/-}$; $Trp53^{pc-/-}$ mice (Figure 4A; see Figure S7A for the FACS characterization of infused cells). One million monocytes were injected intravenously every 3 days for a total of six injections, and tumors were collected the day after the last infusion. Infusion of mCherry-labeled monocytes, and the consequent FACS analysis of the tumor infiltrate, allowed the detection of these cells in the tumor and their differentiation from macrophages (see Figure S7B for the gating strategy). Strikingly, FACS analysis showed that CXCR2-KO monocytes infiltrating the tumor polarized mainly toward pro-inflammatory TAMs and that the frequency of TAMs was similar in both mice infused with CXCR2 WT and CXCR2-KO monocytes (Figures 4B and 4C; Figure S7C). Immunofluorescence staining on tumor sections further showed a significant increase of pro-inflammatory Inos-expressing macrophages upon infusion of CXCR2-KO monocytes (Figures 4D and 4E). Furthermore, RT-qPCR analysis performed on TAMs FACS-sorted from the tumors confirmed the re-education of TAMs toward pro-inflammatory functional state in mice infused with the CXCR2-KO monocytes, as shown by the decreased expression of both CD206 and arginase and increased TNFα expression (Figure 4F). Importantly, infusion of CXCR2-KO but not CXCR2 WT monocytes in $Pten^{pc-/-}$; $Trp53^{pc-/-}$ mice and the resulting enrichment in pro-inflammatory macrophages was associated with a strong tumor inhibition, induction of DNA damage, and senescence response, as shown by immunohistochemistry staining for Ki-67, pH2AX, p16, pHp1γ, and SA-β-galactosidase (Figures 4G–4L; Figures S7D and S7E). Western blot analysis for GATA4 levels further confirmed the induction of a senescence response in these tumors (Figure S7F). Of note, infusion of WT monocytes did not result in tumor growth advantage compared with age-matched tumor-bearing $Pten^{pc-/-}$; $Trp53^{pc-/-}$ untreated mice (Figure 4I). Altogether, these results indicate that inhibition of the CXCR2 receptor in TAMs promotes a re-education of these cells toward a pro-inflammatory state that induces a strong senescence response, even in $Pten^{pc-/-}$; $Trp53^{pc-/-}$-null prostate tumors.

Pro-inflammatory Macrophages Drive Senescence Induction in *PTEN*-Null Cells through TNFα

To broaden the translational relevance of these findings, we next investigated the mechanism by which αCXCR2-treated pro-inflammatory macrophages promote senescence inhuman PTEN-deficient prostate cancer cells. We therefore exposed human epithelial cancer cell lines to the c.m. of TAMs treated in presence or absence of the CXCR2 antagonist (tumor-conditioned macrophages). C.m. from pro-inflammatory (IFNγ/LPS) and anti-inflammatory (IL-4/IL-13) macrophages was used as control. Treatment with c.m. from αCXCR2-treated tumor-conditioned macrophages promoted a strong growth arrest and senescence response specifically in $PTEN^{-/-}$; $TRP53^{+/+}$ LnCaP and $PTEN^{-/-}$; $TRP53^{-/-}$ PC3 cells, while $PTEN^{+/+}$; $TRP53^{+/+}$ 22RV1 control cells were not affected. In line with these findings, c.m. from IFNγ/LPS-treated pro-inflammatory macrophages also induced senescence and cell growth inhibition in LnCaP and PC3 cells, whereas c.m. from IL-4/IL-13-polarized macrophages slightly promoted proliferation in these cells (Figures 5A and 5B). Of note, deletion of *Trp53* did not result in decreased sensitivity of PTEN-null cells to the administration of the c.m. from aCXCR2-TAMs. To then identify factors secreted by pro-inflammatory macrophages affecting the proliferation and senescence of PTEN-deficient cells, we performed an *in vitro* screening in MEFs with cytokines released by *in vitro* derived pro-inflammatory macrophages (Figure S8A). Among all the tested factors, TNFα was the only molecule capable of inducing growth inhibition and senescence in PTEN-null human cancer cells (Figures 5C and 5D) and decreasing tumor growth of

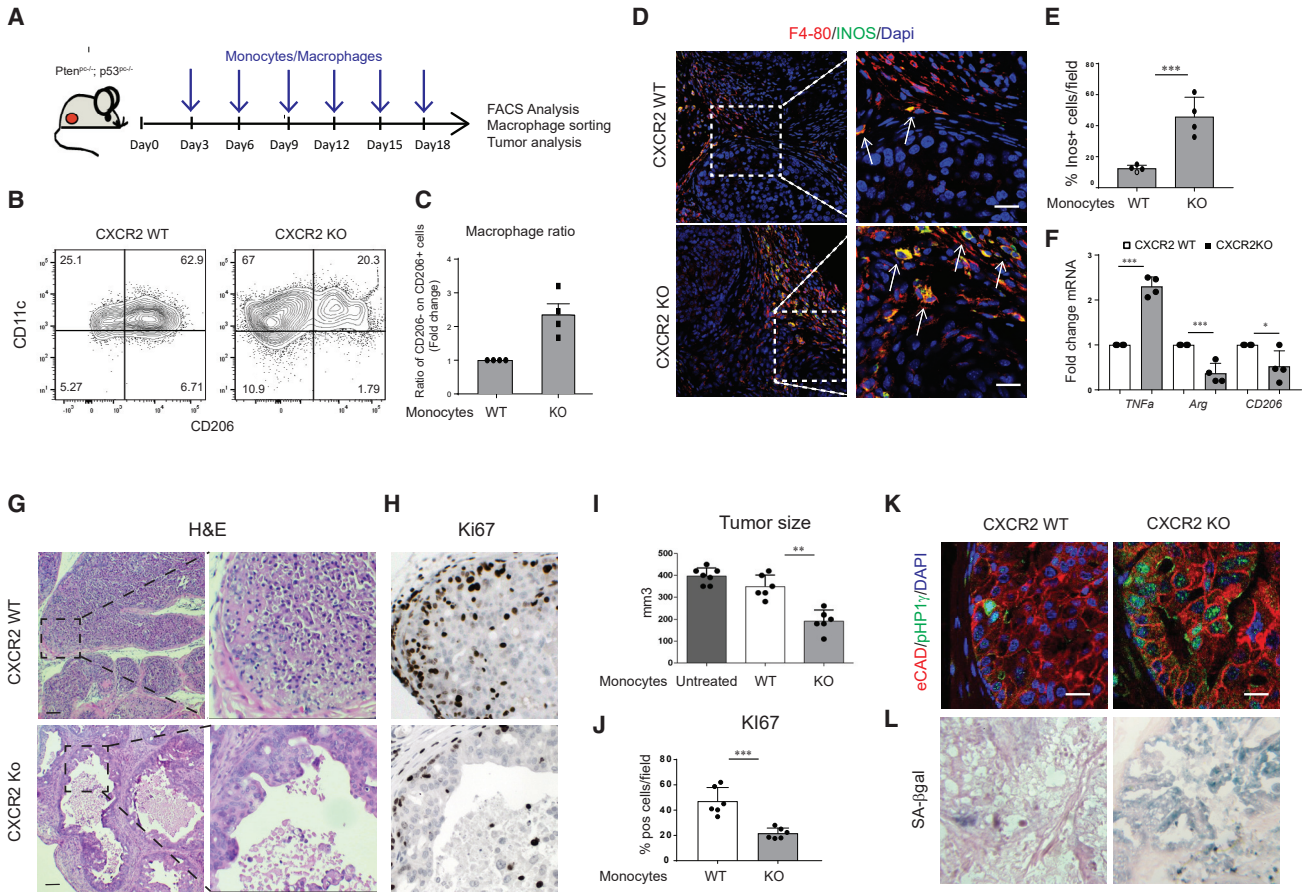

Figure 4. CXCR2-Depleted Monocytes Infusion Drives TAM Re-education and Senescence Induction in *Pten*$^{pc-/-}$; *p53*$^{pc-/-}$ Tumors

(A) Schedule of treatment used in the pre-clinical trial with CXCR2 WT or CXCR2-KO infused monocytes (n = 6 mice per group).

(B and C) Representative FACS plots of immunophenotyping (B) and quantification (C) showing macrophages ratio of CD11c^{+}CD206^{-} pro-inflammatory and CD11c$^{+/-}$ CD206^{+} anti-inflammatory macrophages infiltrating the tumor upon infusion of CXCR2 WT or CXCR2-KO monocytes. Events are gated on CD45^{+}CD11b^{+}F4/80^{+} cells (n = 4 mice per group).

(D and E) Representative confocal immunofluorescence image (D) and quantification (E) of F4/80-positive (red) and Inos-positive (green) tumor-infiltrating macrophages. Cells were counterstained with the nuclear marker DAPI (blue). Scale bar, 15 μM.

(F) RT-qPCR gene expression analysis on CD45^{+}F4/80^{+} macrophages sorted from tumors.

(G–J) H&E (G), Ki-67 IHC staining (original magnification, 20×) (H), relative anterior prostate lobe volume compared with untreated *Pten*$^{pc-/-}$; *p53*$^{pc-/-}$ mice (I), and Ki-67 quantification in *Pten*$^{pc-/-}$; *p53*$^{pc-/-}$ prostatic tumors upon infusion of CXCR2 WT or CXCR2-KO monocytes (J).

(K) Immunofluorescence staining of e-Cadherin-positive (red) and pHP1γ-positive (green) epithelial cells in *Pten*$^{pc-/-}$; *p53*$^{pc-/-}$ prostatic tumors upon infusion of CXCR2 WT or CXCR2-KO monocytes. Cells were counterstained with the nuclear marker DAPI (blue). Scale bar, 20 μm.

(L) Representative images of SA-βgalactosidase IHC staining on *Pten*$^{pc-/-}$; *p53*$^{pc-/-}$ prostatic tumors. Original magnification, 40×. Scale bar, 100 μm.

Error bars are mean ± SEM. **p < 0.01 and ***p < 0.001.

prostate tumor organoids (Figure S8B). These findings were also validated in an isogenic TRAMP-C1 mouse epithelial prostate cancer cell line in which *Pten* was deleted by using a Crispr-Cas9 system (Figures S8C and S8D).

To further dissect the specificity of TNFα for the *PTEN*$^{-/-}$background, we analyzed the mRNA expression levels of *TNFR1* in human prostate cancer cell lines and human tumor organoids. RT-qPCR analysis for *TNFR1*showed the existence of an inverse correlation between the expression of *PTEN* and *TNFR1* in these settings (Figures 5E–5G), thereby potentially explaining the higher sensitivity of *PTEN*$^{-/-}$ cells to TNFα exposure. This was also confirmed in TRAMP-C1-*Pten*$^{-/-}$prostate tumor cells (Figure S8E).

CXCR2 Blockade Reverts the Effect of Anti-CXCR2 Treatment in PTEN-Null Prostate Tumors *In Vivo*

To further investigate the impact of TNFα in tumor treated with anti-CXCR2 antagonist, we treated mice bearing *Pten*$^{-/-}$-TRAMP-C1 allograft tumors with a combination of AZD5069 and a neutralizing antibody for TNFα. Strikingly, the anti-tumorigenic and pro-senescent effect of AZD5069 treatment was reverted upon blockade of TNFα. Indeed, tumor volume was significantly decreased upon administration of the CXCR2 antagonist over time, and its efficacy was dramatically reverted upon TNFα neutralization *in vivo*. These results were further validated in the *Pten*-null-TRAMP-C1 cells in which *TNFR1* was deleted by using a Crispr-Cas9 system (*Pten*-null; *TNFR1*-null-TRAMP-C1). Of

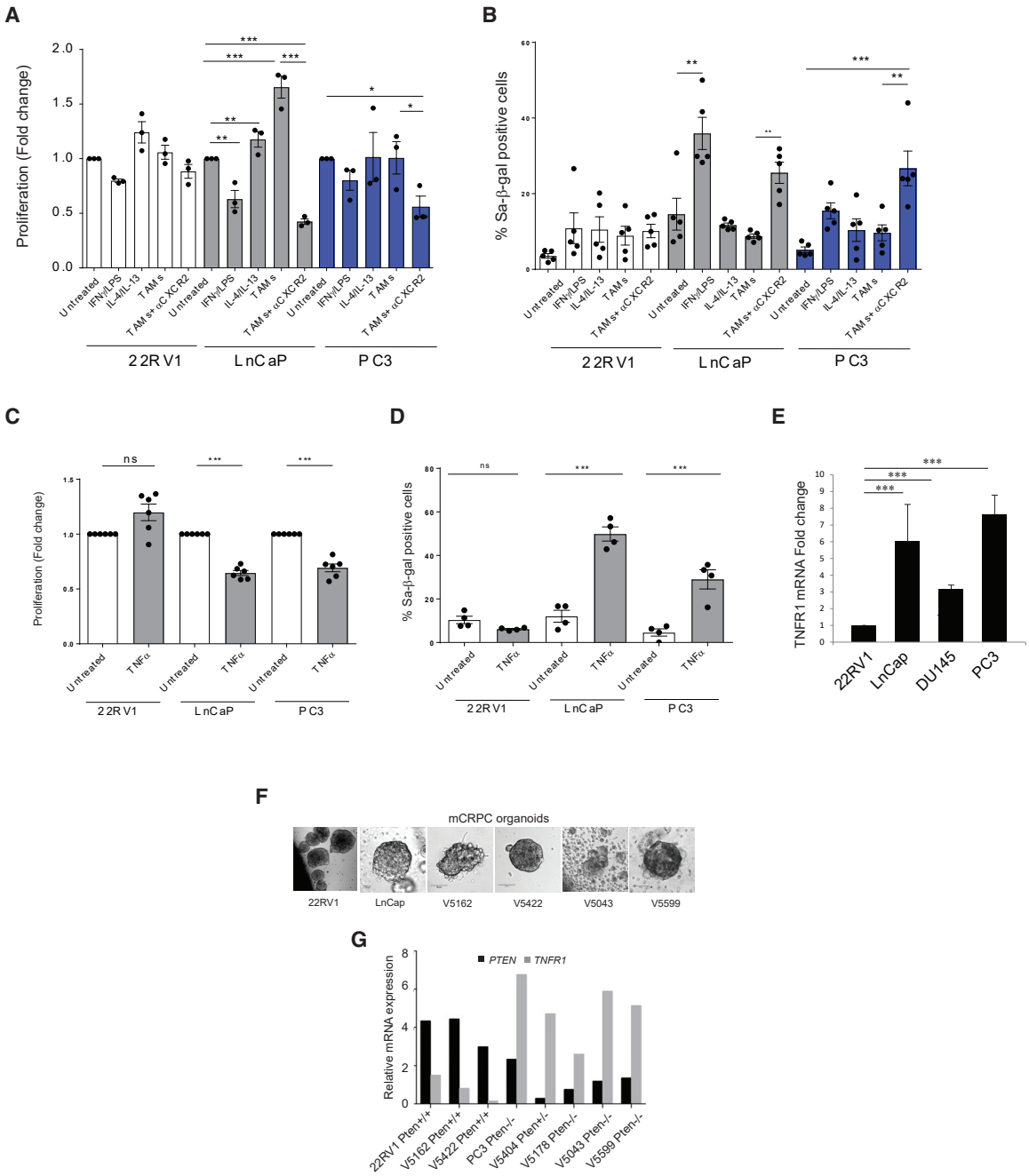

Figure 5. Pro-inflammatory Macrophages Induce Growth Arrest and Senescence Enhancement in *Pten*-Null Tumors

(A and B) Bar graph showing fold change in cell proliferation (A) and percentage (B) of SA-b-galactosidase positive human cancer cells exposed to conditioned media from stimulated macrophages. Macrophages were either untreated or stimulated with the following: IFNγ/LPS, IL-4/IL-13, and conditioned media from PC3 cancer cells ± aCXCR2.

(C and D) Bar graph showing fold change in cell proliferation (C) and percentage (D) of SA-b-galactosidase positive cells from 22Rv1, LnCaP, and PC3 treated with recombinant TNFα.

(E) RT-qPCR analysis of TNFR1 expression in the three human cell lines.

(F) Bright-field images from three-dimensional (3D) culture of CRPC patient-derived organoids and cell line-derived organoids (hanging drop) acquired with Zeiss LSM700 confocal laser scanning microscope.

(G) RT-qPCR analysis showing the anti-correlation of *PTEN* and *TNFR1* relative expression in human mCRPC patient-derived organoids. Bar chart showing fold change comparison between each gene in reference to a *PTEN* +/+ control (22Rv1) and *Lamin A/C* used as a housekeeping gene.

Error bars are mean ± SEM (n = 2). *p < 0.05, **p = 0.0071 (two-way ANOVA), and ***p < 0.001.

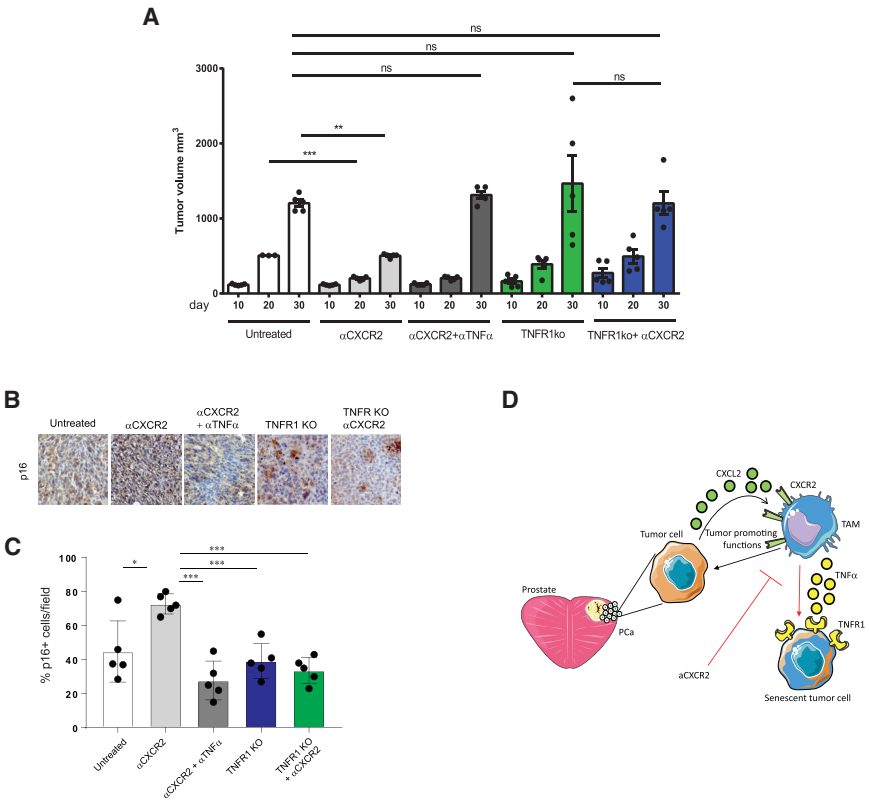

Figure 6. TNFα Neutralization Disrupts the Efficacy of CXCR2 Blockade in Syngeneic Prostate Tumors *In Vivo*

For the allograft experiments, 2.5 × 10^6 TRAMP-C1 cells were injected subcutaneously into the flank of male C57BL/6 mice. When tumors were approximately 200 mm^3, mice were randomized to the treatment groups. Tumor growth was monitored daily by measuring the tumor size with caliper. Mice were treated with αCXCR2 (AZD5069 100 mg/kg) daily for 3 weeks.

(A) Bar graph showing the relative tumor volume (mm^3) at days 10, 20, and 30 after injection in mice bearing TRAMPTRAMP-C1C1 Pten−/−; Trp53−/− allografts treated with αCXCR2 with or without combination with a monoclonal antibody for TNFα. The graph is also showing the tumor size of Pten−/−; Trp53−/− TNFR1−/− TRAMP-C1 cells in the presence or absence of αCXCR2 treatment, at the same time points. CRISPR/Cas9 was performed on TRAMP-C1 cells to delete *TNFR1*.

(B and C) Representative images of IHC staining (B) and quantification (C) of p16 in all the conditions.

(D) Schematic model showing the mechanism by which CXCR2 blockade reprograms TAMs in prostate tumors.

Error bars are mean ± SEM. *p < 0.05, **p < 0.01, and ***p < 0.001.

note, tumor size of *Pten*-null-TRAMP-C1 cells injected in hosting mice was not affected by AZD5069 treatment in cells depleted from the TNFR1, thus confirming the role played by TNFα in mediating the efficacy of the CXCR2 antagonist (Figure 6A). Furthermore, in accordance with the pro-senescent effect exerted by TNFα-releasing macrophages in *Pten*$^{-/-}$ cancers, TNFα neutralization and *TNFR1* inactivation in *Pten*-null-TRAMP-C1 tumors resulted in the inhibition of senescence, as shown by a decreased expression of p16 levels in these tumors (Figures 6B and 6C).

DISCUSSION

Altogether our findings disclose the mechanism by which CXCR2 antagonists exert an antitumor response. Here we show that the majority of TAMs infiltrating *Pten*-null prostate cancer expressed the C-X-C chemokine receptor type 2 (CXCR2). Pharmacological blockade of the CXCR2 receptor in tumor models *in vivo*, by a selective antagonist, promoted the re-education of TAMs toward a TNFα-releasing pro-inflammatory phenotype, which resulted in induction of senescence and tumor inhibition. Dissection of the mechanisms by which TAMs affect tumor progression has paved the way for the development of macrophage-targeting therapies. Indeed, multiple therapeutic strategies aimed at TAMs depletion have been developed. Among those, α-CSF-1R monoclonal antibodies have been shown to alter macrophage frequency in models of colorectal adenocarcinoma and fibrosarcoma (Ries et al., 2014). In addition, depletion of TAMs has been demonstrated to be a key mechanism mediating the anti-tumor activity of trabectedin in human liposarcoma (Germano et al., 2013). Importantly, recent findings also support the possibility to activate the anti-tumor activity of TAMs in cancer, rather than blocking their recruitment or localization. Administration of an agonistic α-CD40 antibody in a model of pancreatic cancer resulted in the re-education of TAMs toward a pro-inflammatory phenotype, leading to a reduction in tumor volume (Beatty et al., 2013). Furthermore, reprogramming of tumor-infiltrating macrophages toward an anti-cancer phenotype has also been achieved in murine tumor models through class IIa HDAC inhibition and via the expression of antiangiogenic and immunomodulatory protein histidine-rich glycoprotein (HRG) (Guerriero et al., 2017; Rolny et al., 2011). In this regard, in the present study, we took advantage of the AZD5069, a CXCR2 antagonist that, in contrast to therapies that deplete TAMs in tumors, blocks tumorigenesis by re-educating the TAMs toward an anti-tumorigenic and pro-senescent functional state without affecting the total number of TAMs in the tumor microenvironment. Given that the macrophage represents the most prominent population infiltrating the tumor in most cancers, our strategy may permit exploitation of the localization of macrophages at the tumor bed by triggering their anti-tumorigenic power. Interestingly, here we show that members of the CXCL family, known to bind the CXCR2 receptor, were increased in prostate cancer and correlate with cancer progression, thus supporting previous evidence demonstrating that the CXCL-CXCR pathway plays a substantial role in tumor development and further

indicating that developing effective therapies aimed at the disruption of such pathway may be critical for tumor treatment in many cancer types. In addition, our findings provide evidence that support the use of autologous infusion of monocytes as a therapy for prostate cancer. Indeed, our findings show that infusion of CXCR2-KO monocytes in tumor-bearing animals resulted in tumor inhibition and senescence induction, accompanied by the re-education of the infiltrating macrophages toward a pro-inflammatory state. Of note, autologous infusion of human activated monocytes was attempted in the past but resulted in poor clinical response in cancer-bearing patients. Importantly, significant levels of pro-inflammatory cytokines were never detected in the serum of treated patients after monocytes infusions (Lopez et al., 1992, 1994; Stevenson et al., 1988), suggesting that activated monocytes were reprogrammed toward an anti-inflammatory and therefore pro-tumorigenic phenotype once infused. Our results show that a more efficient strategy could be achieved in the clinic by combining infusion of monocytes with the αCXCR2 treatment, as this combination will skew the monocytes and derived macrophages toward an anti-tumorigenic functional state. Finally, given that CXCR2 antagonists are currently being evaluated in the clinic to treat different types of tumor, including prostate cancer, it will be imperative to investigate the clinical settings in which these compounds may have the largest impact. In this regard, our results indicate that tumors harboring *Pten* deletion are sensitive to αCXCR2 treatment and to the consequent TNFα-induced senescence, as these tumor cells upregulate *TNFR1* (Figure 6D). Previous evidence supported the role of TNFα in triggering apoptosis of tumor cells and senescence induction (Beyne-Rauzy et al., 2004; Dumont et al., 2000; Guerriero et al., 2017). However, whether TNFα is capable to induce an antitumor response may depend on the genetic background of the tumors, as in certain tumor types, TNFα does not affect tumor growth and even increases tumorigenesis (Braumüller et al., 2013; Waters et al., 2013). Thus, clinical trials evaluating the efficacy of CXCR2 antagonists should take into account this information, and treated patients should be stratified for the level of *PTEN* in the tumors.

STAR★METHODS

Detailed methods are provided in the online version of this paper and include the following:

SUPPLEMENTAL INFORMATION

Supplemental Information can be found online at https://doi.org/10.1016/j.celrep.2019.07.068.

ACKNOWLEDGMENTS

We thank all members of the IRB animal core facility for technical assistance and animal work. We thank Dr. D. Jarrossay for helping with the cell sorting experiments. We thank all members of the Dr. A. Alimonti laboratory for scientific discussions. This work was supported by a European Research Council (ERC) starting grant (261342) and an ERC consolidator (683136); grants from the Josef Steiner Foundation, the Helmut Horten Foundation, and Krebsliga (KFS 3505-08-2014); SNF (Ambizione) (PZ00P3_136612); and an AIRC Start-Up grant 2016 (19141).

AUTHOR CONTRIBUTIONS

A.A. and D.D. developed the concept and designed the experiments. D.D., M. Mirenda, J.V., A.C., V.G., G.B., E.P., and A. Rinaldi performed experiments. D.D., N.D., G.C., P.O., and A. Rinaldi performed the gene expression-related experiments and analyzed the data. D.D., J.V., R.D., and M. Masetti established and carried out fluorescence microscopy. M.L. and S.M. performed immunohistochemical experiments and analysis. M.G. provided the EC cell line. L.G., D.W., and R.P.M. provided and analyzed the TMA and samples from prostate cancer patients. S.B. provided the AZD5069 compound. J.D.B. supervised the organoid experiments and interpreted the data. D.D., M. Mirenda, and A.A. interpreted the data. D.D. and A.A. wrote the paper.

DECLARATION OF INTERESTS

S.B. is employed in the Oncology Department of AstraZeneca, Li KaShing Centre, Cambridge, UK. A.A. and J.D.B. have received a research grant from AstraZeneca for the clinical development of AZD5069. J.D.B. has served on advisory boards for many companies, including AstraZeneca, Astellas, Bayer, Boehringer Ingelheim, Genentech/Roche, Genmab, GlaxoSmithKline, Janssen, Merck Serono, Merck Sharp & Dohme, Menarini/Silicon Biosystems, Orion, Pfizer, Sanofi-Aventis, and Taiho. The ICR has a commercial interest in abiraterone, PARP inhibition in DNA repair-defective cancers, and PI3K/AKT pathway inhibitors (no personal income). The ICR has received funding or other support for my research work from AstraZeneca, Astellas, Bayer, Genentech, GlaxoSmithKline, Janssen, Merck Serono, Merck Sharp & Dohme, Menarini/Silicon Biosystems, Orion, Sanofi-Aventis, and Taiho. J.D.B. has been the chief investigator (CI) or principal investigator (PI) of many industry sponsored clinical trials. All the other authors declare no competing interests.

Received: December 5, 2018
Revised: June 5, 2019
Accepted: July 18, 2019
Published: August 20, 2019

REFERENCES

Alimonti, A., Carracedo, A., Clohessy, J.G., Trotman, L.C., Nardella, C., Egia, A., Salmena, L., Sampieri, K., Haveman, W.J., Brogi, E., et al. (2010). Subtle variations in Pten dose determine cancer susceptibility. Nat. Genet. *42*, 454–458.

Baer, C., Squadrito, M.L., Laoui, D., Thompson, D., Hansen, S.K., Kiialainen, A., Hoves, S., Ries, C.H., Ooi, C.H., and De Palma, M. (2016). Suppression of microRNA activity amplifies IFN-γ-induced macrophage activation and promotes anti-tumour immunity. Nat. Cell Biol. *18*, 790–802.

Beatty, G.L., Torigian, D.A., Chiorean, E.G., Saboury, B., Brothers, A., Alavi, A., Troxel, A.B., Sun, W., Teitelbaum, U.R., Vonderheide, R.H., et al. (2013). A phase I study of an agonist CD40 monoclonal antibody (CP-870,893) in combination with gemcitabine in patients with advanced pancreatic ductal adenocarcinoma. Clin. Cancer Res. *19*, 6286–6295.

Beyne-Rauzy, O., Recher, C., Dastugue, N., Demur, C., Pottier, G., Laurent, G., Sabatier, L., and Mansat-De Mas, V. (2004). Tumor necrosis factor alpha induces senescence and chromosomal instability in human leukemic cells. Oncogene *23*, 7507–7516.

Bingle, L., Brown, N.J., and Lewis, C.E. (2002). The role of tumour-associated macrophages in tumour progression: implications for new anticancer therapies. J. Pathol. *196*, 254–265.

Braumüller, H., Wieder, T., Brenner, E., Aßmann, S., Hahn, M., Alkhaled, M., Schilbach, K., Essmann, F., Kneilling, M., Griessinger, C., et al. (2013). T-helper-1-cell cytokines drive cancer into senescence. Nature *494*, 361–365.

Calcinotto, A., Spataro, C., Zagato, E., Di Mitri, D., Gil, V., Crespo, M., De Bernardis, G., Losa, M., Mirenda, M., Pasquini, E., et al. (2018). IL-23 secreted by myeloid cells drives castration-resistant prostate cancer. Nature *559*, 363–369.

Cassetta, L., Fragkogianni, S., Sims, A.H., Swierczak, A., Forrester, L.M., Zhang, H., Soong, D.Y.H., Cotechini, T., Anur, P., Lin, E.Y., et al. (2019). Human tumor-associated macrophage and monocyte transcriptional landscapes reveal cancer-specific reprogramming, biomarkers, and therapeutic targets. Cancer Cell *35*, 588–602.

Chen, Z., Trotman, L.C., Shaffer, D., Lin, H.K., Dotan, Z.A., Niki, M., Koutcher, J.A., Scher, H.I., Ludwig, T., Gerald, W., et al. (2005). Crucial role of p53-dependent cellular senescence in suppression of Pten-deficient tumorigenesis. Nature *436*, 725–730.

Delaleu, N., Nguyen, C.Q., Tekle, K.M., Jonsson, R., and Peck, A.B. (2013). Transcriptional landscapes of emerging autoimmunity: transient aberrations in the targeted tissue's extracellular milieu precede immune responses in Sjögren's syndrome. Arthritis Res. Ther. *15*, R174.

Dumont, P., Balbeur, L., Remacle, J., and Toussaint, O. (2000). Appearance of biomarkers of in vitro ageing after successive stimulation of WI-38 fibroblasts with IL-1alpha and TNF-alpha: senescence associated beta-galactosidase activity and morphotype transition. J. Anat. *197*, 529–537.

Escamilla, J., Schokrpur, S., Liu, C., Priceman, S.J., Moughon, D., Jiang, Z., Pouliot, F., Magyar, C., Sung, J.L., Xu, J., et al. (2015). CSF1 receptor targeting in prostate cancer reverses macrophage-mediated resistance to androgen blockade therapy. Cancer Res. *75*, 950–962.

Fleetwood, A.J., Dinh, H., Cook, A.D., Hertzog, P.J., and Hamilton, J.A. (2009). GM-CSF- and M-CSF-dependent macrophage phenotypes display differential dependence on type I interferon signaling. J. Leukoc. Biol. *86*, 411–421.

Germano, G., Frapolli, R., Belgiovine, C., Anselmo, A., Pesce, S., Liguori, M., Erba, E., Uboldi, S., Zucchetti, M., Pasqualini, F., et al. (2013). Role of macrophage targeting in the antitumor activity of trabectedin. Cancer Cell *23*, 249–262.

Guerriero, J.L., Sotayo, A., Ponichtera, H.E., Castrillon, J.A., Pourzia, A.L., Schad, S., Johnson, S.F., Carrasco, R.D., Lazo, S., Bronson, R.T., et al. (2017). Class IIa HDAC inhibition reduces breast tumours and metastases through anti-tumour macrophages. Nature *543*, 428–432.

Hagemann, T., Biswas, S.K., Lawrence, T., Sica, A., and Lewis, C.E. (2009). Regulation of macrophage function in tumors: the multifaceted role of NF-kappaB. Blood *113*, 3139–3146.

Kaneda, M.M., Messer, K.S., Ralainirina, N., Li, H., Leem, C.J., Gorjestani, S., Woo, G., Nguyen, A.V., Figueiredo, C.C., Foubert, P., et al. (2016). PI3Kγ is a molecular switch that controls immune suppression. Nature *539*, 437–442.

Kang, C., Xu, Q., Martin, T.D., Li, M.Z., Demaria, M., Aron, L., Lu, T., Yankner, B.A., Campisi, J., and Elledge, S.J. (2015). The DNA damage response induces inflammation and senescence by inhibiting autophagy of GATA4. Science *349*, aaa5612.

Lanciotti, M., Masieri, L., Raspollini, M.R., Minervini, A., Mari, A., Comito, G., Giannoni, E., Carini, M., Chiarugi, P., and Serni, S. (2014). The role of M1 and M2 macrophages in prostate cancer in relation to extracapsular tumor extension and biochemical recurrence after radical prostatectomy. BioMed Res. Int. *2014*, 486798.

Lopez, M., Fechtenbaum, J., David, B., Martinache, C., Chokri, M., Canepa, S., De Gramont, A., Louvet, C., Gorin, I., Mortel, O., et al. (1992). Adoptive immunotherapy with activated macrophages grown in vitro from blood monocytes in cancer patients: a pilot study. J. Immunother. *11*, 209–217.

Lopez, M., Louvet, C., Martinache, C., Bony, V., Scotto, F., Barelaud, S., Jiang, R., Drapier, J.C., Smadja, V., De Gramont, A., et al. (1994). Infusion of large quantities of autologous blood monocyte-derived macrophages in two cancer patients did not induce increased concentration of IL-6, TNF-alpha, soluble CD14 and nitrate in blood plasma. Eur. Cytokine Netw. *5*, 411–414.

Mantovani, A., Schioppa, T., Porta, C., Allavena, P., and Sica, A. (2006). Role of tumor-associated macrophages in tumor progression and invasion. Cancer Metastasis Rev. *25*, 315–322.

Mantovani, A., Marchesi, F., Malesci, A., Laghi, L., and Allavena, P. (2017). Tumour-associated macrophages as treatment targets in oncology. Nat. Rev. Clin. Oncol. *14*, 399–416.

Martinez, F.O., and Gordon, S. (2014). The M1 and M2 paradigm of macrophage activation: time for reassessment. F1000Prime Rep. *6*, 13.

Mazzieri, R., Pucci, F., Moi, D., Zonari, E., Ranghetti, A., Berti, A., Politi, L.S., Gentner, B., Brown, J.L., Naldini, L., and De Palma, M. (2011). Targeting the ANG2/TIE2 axis inhibits tumor growth and metastasis by impairing angiogenesis and disabling rebounds of proangiogenic myeloid cells. Cancer Cell *19*, 512–526.

Mosser, D.M., and Edwards, J.P. (2008). Exploring the full spectrum of macrophage activation. Nat. Rev. Immunol. *8*, 958–969.

Murray, P.J., Allen, J.E., Biswas, S.K., Fisher, E.A., Gilroy, D.W., Goerdt, S., Gordon, S., Hamilton, J.A., Ivashkiv, L.B., Lawrence, T., et al. (2014). Macrophage activation and polarization: nomenclature and experimental guidelines. Immunity *41*, 14–20.

Nava Rodrigues, D., Rescigno, P., Liu, D., Yuan, W., Carreira, S., Lambros, M.B., Seed, G., Mateo, J., Riisnaes, R., Mullane, S., et al. (2018). Immunogenomic analyses associate immunological alterations with mismatch repair defects in prostate cancer. J. Clin. Invest. *128*, 4441–4453.

Nonomura, N., Takayama, H., Kawashima, A., Mukai, M., Nagahara, A., Nakai, Y., Nakayama, M., Tsujimura, A., Nishimura, K., Aozasa, K., and Okuyama, A. (2010). Decreased infiltration of macrophage scavenger receptor-positive cells in initial negative biopsy specimens is correlated with positive repeat biopsies of the prostate. Cancer Sci. *101*, 1570–1573.

Patnaik, A., Swanson, K.D., Csizmadia, E., Solanki, A., Landon-Brace, N., Gehring, M.P., Helenius, K., Olson, B.M., Pyzer, A.R., Wang, L.C., et al. (2017). Cabozantinib eradicates advanced murine prostate cancer by activating antitumor innate immunity. Cancer Discov. *7*, 750–765.

Pienta, K.J., Machiels, J.P., Schrijvers, D., Alekseev, B., Shkolnik, M., Crabb, S.J., Li, S., Seetharam, S., Puchalski, T.A., Takimoto, C., et al. (2013). Phase 2 study of carlumab (CNTO 888), a human monoclonal antibody against CC-chemokine ligand 2 (CCL2), in metastatic castration-resistant prostate cancer. Invest. New Drugs *31*, 760–768.

Pyonteck, S.M., Akkari, L., Schuhmacher, A.J., Bowman, R.L., Sevenich, L., Quail, D.F., Olson, O.C., Quick, M.L., Huse, J.T., Teijeiro, V., et al. (2013).

CSF-1R inhibition alters macrophage polarization and blocks glioma progression. Nat. Med. *19*, 1264–1272.

Qian, B.Z., and Pollard, J.W. (2010). Macrophage diversity enhances tumor progression and metastasis. Cell *141*, 39–51.

Rath, M., Müller, I., Kropf, P., Closs, E.I., and Munder, M. (2014). Metabolism via arginase or nitric oxide synthase: two competing arginine pathways in macrophages. Front. Immunol. *5*, 532.

Ries, C.H., Cannarile, M.A., Hoves, S., Benz, J., Wartha, K., Runza, V., Rey-Giraud, F., Pradel, L.P., Feuerhake, F., Klaman, I., et al. (2014). Targeting tumor-associated macrophages with anti-CSF-1R antibody reveals a strategy for cancer therapy. Cancer Cell *25*, 846–859.

Rolny, C., Mazzone, M., Tugues, S., Laoui, D., Johansson, I., Coulon, C., Squadrito, M.L., Segura, I., Li, X., Knevels, E., et al. (2011). HRG inhibits tumor growth and metastasis by inducing macrophage polarization and vessel normalization through downregulation of PlGF. Cancer Cell *19*, 31–44.

Salvagno, C., Ciampricotti, M., Tuit, S., Hau, C.S., van Weverwijk, A., Coffelt, S.B., Kersten, K., Vrijland, K., Kos, K., Ulas, T., et al. (2019). Therapeutic targeting of macrophages enhances chemotherapy efficacy by unleashing type I interferon response. Nat. Cell Biol. *21*, 511–521.

Starr, T., Bauler, T.J., Malik-Kale, P., and Steele-Mortimer, O. (2018). The phorbol 12-myristate-13-acetate differentiation protocol is critical to the interaction of THP-1 macrophages with Salmonella Typhimurium. PLoS ONE *13*, e0193601.

Steele, C.W., Karim, S.A., Leach, J.D.G., Bailey, P., Upstill-Goddard, R., Rishi, L., Foth, M., Bryson, S., McDaid, K., Wilson, Z., et al. (2016). CXCR2 inhibition profoundly suppresses metastases and augments immunotherapy in pancreatic ductal adenocarcinoma. Cancer Cell *29*, 832–845.

Stevenson, H.C., Lacerna, L.V., Jr., and Sugarbaker, P.H. (1988). Ex vivo activation of killer monocytes (AKM) and their application to the treatment of human cancer. J. Clin. Apher. *4*, 118–121.

Su, G., Morris, J.H., Demchak, B., and Bader, G.D. (2014). Biological network exploration with Cytoscape 3. Curr. Protoc. Bioinformatics *47*, 8.13.1–8.13.24.

Takeda, K., Tanaka, T., Shi, W., Matsumoto, M., Minami, M., Kashiwamura, S., Nakanishi, K., Yoshida, N., Kishimoto, T., and Akira, S. (1996). Essential role of Stat6 in IL-4 signalling. Nature *380*, 627–630.

Waters, J.P., Pober, J.S., and Bradley, J.R. (2013). Tumour necrosis factor and cancer. J. Pathol. *230*, 241–248.

STAR★METHODS

KEY RESOURCES TABLE

REAGENT or RESOURCE	SOURCE	IDENTIFIER
Antibodies		
CD3ε (Clone 145-2C11)	Biolegend	Cat# 100434; Lot. B241616; RRID:AB_893324
CD4 (Clone GK1.5)	Biolegend	Cat# 100434; Lot. B248433; RRID:AB_893324
CD8a (Clone 53-6.7)	Biolegend	Cat# 100741; Lot. B272200; RRID:AB_11124344
CD11b (Clone M1/70)	Biolegend	Cat# 101235; Lot. B251703; RRID:AB_10897942
CD45 (Clone 30-F11)	Biolegend	Cat# 103155; Lot. B253523; RRID:AB_2650656
Ly6C (Clone HK1.4)	Invitrogen	Ref. 25-5932-82; Lot. 1990189; RRID: AB_1724153
Ly6G (Clone 1A8)	BD	Cat# 551459; Lot. 21064; RRID:AB_394206
NK 1.1 (Clone PK136)	Invitrogen	Ref. 17-5941-81; Lot. 2003461; RRID: AB_469479
CD206 (Clone C068C2)	Biolegend	Cat# 141707; Lot. B230155; RRID:AB_10896057
F4/80 (Clone BM8)	Invitrogen	Ref. 47-4801-80; Lot. 4338512; RRID: AB_1548745
Gr1 (Clone RB6-8C5)	Invitrogen	Ref. 12-5931-81; Lot. 4335548; RRID: AB_466045
B220 (Clone RA3-6B2)	Biolegend	Cat# 103222; Lot. B24773; RRID:AB_313005
CXCR2 (Clone SA045E1)	Biolegend	Cat# 149609; Lot. B258930; RRID:AB_2565689
TNF-a (Clone MP6-XT22)	Biolegend	Cat# 506307; Lot. B230018; RRID:AB_315428
Granzyme B (Clone GB11)	Biolegend	Cat# 515407; Lot. B260874; RRID:AB_2562195
Purified anti-mouse CD16/32 (Clone 93)	Biolegend	Cat# 101301; Lot. B264872; RRID:AB_312800
Dynabeads mouse T activator CD3/CD28	GIBCO By ThermoFisher	Ref. 11452D; Lot. 00758725
Cell Trace Violet Cell Proliferation Kit	Invitrogen	Cat. C34557; Lot. 1851453
GATA-4 (D3A3M)	Cell Signaling	36966; RRID: AB_2799108
HSP-90 (C45G5)	Cell Signaling	4877S; RRID: AB_2233307
PTEN	Cell Signaling	552S; RRID: AB_390810
a-TUBULIN (9F3)	Cell Signaling	2128; RRID: AB_1950376
p-STAT6 (Tyr641) (D8S9Y)	Cell Signaling	56554; RRID: AB_2799514
STAT-6	Cell Signaling	9362s; RRID: AB_2271211
TNFR1 (D3I7K)	Cell Signaling	13377S; RRID: AB_2798194
Chemicals, Peptides, and Recombinant Proteins		
Human Recombinant IL-13	Peprotech	Cat. AF-200-13; Lot. 0512AFC23 H1913
Human Recombinant IL-4	Peprotech	Cat. AF-200-04; Lot. 0712AFC14 G1218
Human Recombinant IFN-g	Peprotech	Cat. AF-300-02; Lot. 0412 AFC27
Mouse Recombinant IFN-g	Peprotech	Cat. 315-05; Lot. 061398
Mouse Recombinant CXCR2	Peprotech	Cat. 250-15; Lot. 098152 E0913
Mouse Recombinant IL-4	Peprotech	Cat. 214-14; Lot. 081449 K1915
Mouse Recombinant IL-13	Peprotech	Cat. 210-13; Lot. 1111207
BD Golgi Plug	BD	Cat. 51-230 1KZ; Lot. 4309737-1
PMA (Phorbol 12-myristate 13-acetate)	Sigma-Aldrich	Cat. P8139-1MG
Ionomycin	Sigma-Aldrich	Cat. I0634
Dnase I	Sigma-Aldrich	Cat. 4716728001
Anti human TNF-a (recombinant)	Peprotech	Cat. AF-300-01A; Lot. 0609AFC25
Anti mouse-TNF-a (Recombinant)	Peprotech	Cat. 500-P64; Lot. 1111207
Critical Commercial Assays		
Senescence β-Galactosidase Staining Kit	Cell Signaling Technology	Cat. #9860S
Proteome Profiler Mouse Cytokine Array Kit, Panel A	R&D Systems	Cat. ARY006

(*Continued on next page*)

Continued

REAGENT or RESOURCE	SOURCE	IDENTIFIER
EasySep PE Positive Selection Kit II	Stem Cell Technology	Catalog # 17684
Deposited Data		
Raw RNA-Seq Data	This Paper	GEO accession number: GSE125273 https://www.ncbi.nlm.nih.gov/geo/query/acc.cgi?acc=GSE125273
Experimental Models: Cell Lines		
LNCap/C4	ATCC	ATCC® CRL-3313
PC3	ATCC	ATCC® CRL-1435
22RV1	ATCC	ATCC® CRL-2505
TRAMP-C1	ATCC	ATCC® CRL-2730
THP-1	ATCC	ATCC® TIB-202
Experimental Models: Organisms/Strains		
Mouse; C57BL/6NCrl	Charles River	Strain Code: 027
Mouse; *Pten*$^{pc-/-}$ (C57BL/6J background)	Donation from the laboratory of Prof. Pier Paolo Pandolfi (Harvard)	N/A
Mouse; *Pten*$^{pc-/-}$; *Trp53*$^{pc-/-}$ (C57BL/6J background)	Donation from the laboratory of Prof. Pier Paolo Pandolfi (Harvard)	N/A
Oligonucleotides		
PTEN CRISPR/Cas9 KO Plasmid (m)	Santa Cruz Biotechnology	sc-422475
TNFR1 CRISPR/Cas9 KO Plasmid (m)	Santa Cruz Biotechnology	sc-423442-KO-2
RT-qPCR primers, see Table S1	"this paper"	Sigma Aldrich
Software and Algorithms		
Flow Jo_v10	Tree Star	https://flowjo.com/
ImageJ	NIH	https://imagej.nih.gov/ij/
Cytoscape	Cytoscape	https://cytoscape.org/
Graph Pad Prism	GraphPad Software	https://www.graphpad.com

LEAD CONTACT AND MATERIALS AVAILABILITY

There are restrictions to the availability of the following reagent: goat polyclonal anti-pSTAT6 (sc-11762, Santa Cruz Biotechnology). The reagent has been discontinued. Further information and requests for resources and reagents may be directed to and will be fulfilled by Lead Contact, Prof. Andrea Alimonti (andrea.alimonti@ior.usi.ch).

EXPERIMENTAL MODEL AND SUBJECT DETAILS

Mice

All mice were maintained under specific pathogen-free conditions of the IRB institute and experiments were performed according to state guidelines and approved by the local ethical committee ("Dipartimento della Sanità e Socialità, Esperimenti su animali," Canton Ticino). *Pten*$^{pc+/+}$, *Pten*$^{pc-/-}$ and *Pten*$^{pc-/-}$; *Trp53*$^{pc-/-}$ mice (C57BL/6J background) were generated and genotyped as previously described[12]. Female *Pten*$^{loxP/loxP}$ *and* female *Pten*$^{loxP/loxP}$; *Trp53*$^{loxP/loxP}$ mice were crossed with male *PB-Cre4* transgenic mice and genotyped for Cre using following primers, primer1 (5′ TGATGGACATGTTCAGGGATC 3′) and primer2 (5′ CAGCCACCAGCTT GCATGA 3′). B6.129S2(C)-*Cxcr2*^{tm1Mwm}/J (CXCR2 KO) mice were purchased from Jackson laboratory (Stock No: 006848). For the allograft experiments, 2.5x10^6 TRAMP-C1 cells were injected subcutaneously into the flank of male C57BL/6N mice. When tumors were approximately 200 mm^3, mice were randomized to the treatment groups. Tumor growth was monitored daily by measuring the tumor size with caliper. In some experiments mice were treated with intraperitoneal injections of 100 μL of the vehicle or 100 μL αCXCR2 (AZD5069) from Astrazeneca, at a final concentration of 100mg/kg daily for a period of 3 weeks. For the anti-TNFα treatment, mice were injected intraperitoneally with the InVivoMAb anti-mouse TNFα from BioXCell (XT3.11) for a period of 3 weeks, 3 times a week. In some experiments mice were infused with bone marrow derived macrophages (BMDMs), differentiated *in vitro* as previously described (Murray et al., 2014). BMDMs were obtained from male donor CXCR2 WT mice or CXCR2 KO mice. Mice received 1x10^6 BMDMs for intravenous injection. Injections were administered every 3 days for a period of 2 weeks. Recipient mice were sacrificed 1 day post the last injection.

Cells

Primary MEFs (Mouse Embrionic Fibroblasts) were derived from littermate embryos and obtained by crossing *Pten*$^{lx/lx}$ and *Pten*$^{lx/lx}$; *Trp53*$^{lx/lx}$ animals as previously described. Embryos were harvested at 13.5 days post coitum and individual MEFs were produced and cultured as previously described (Chen et al., 2005). Both female and male derived MEFs were utilized. At passage 2 cells were harvested for protein blot analysis. The LnCap (C4), 22Rv1 and PC3 cell lines were purchased from the American Type Culture Collection (ATCC). Cells were maintained at 5% CO2 at 37°C and cultured in RPMI with 10% heat inactivated FBS. All the human cell lines were used for *in vitro* experiments. The TRAMP-C1 cell line was purchased from American Type Culture Collection (ATCC). Cells were maintained at 5% CO2 at 37°C and cultured in DMEM with 10% heat inactivated FBS. For the allograft experiments, 2.5x10^6 TRAMP-C1 cells were injected subcutaneously into the flank of male C57BL/6N mice. The human monocytic cell line THP-1 was used to obtain human macrophages upon differentiation. Cells were maintained at 5% CO2 at 37°C and cultured in RPMI with 10% heat inactivated FBS. THP-1 cells were treated for 24 h with 100 ng/ml PMA to obtain differentiated macrophages(Starr et al., 2018). On the next day cells were washed and media was replaced.

CRISPR-Cas9 transfection

TRAMP-C1 cells were maintained in 75 cm^2 flask to a 50%–60% confluency in DMEM media supplemented with 10% heat-inactivated FBS, 100 U/ml penicillin, 0.1 mg/ml streptomycin and 2 mM L-glutamine. The transfection of the PTEN CRISPR/Cas9 KO plasmid (Santa Cruz Biotechnology) was performed using jetPRIME® transfection reagent according the manufactory protocol at the 1:2 DNA / jetPRIME® ratio. 24h after transfection, the GFP transduced cells were sorted to purity 99% and plated as single cell on 96-well plates. At day 7 after cell sorting the grown cell colonies were moved into 24-well plates for further expansion. The knock-down of *Pten* gene in each cell colony was confirmed by RT-qPCR and western blot.

Human organoids

Organoids were grown in 3D Matrigel® (cat.356231, Corning) under prostate epithelial conditions and lysed directly onto wells and RNA was purified using the Zymo-Spin Columns. RNA was extracted from 3D cultured organoids using Quick-RNA MicroPrep (cat.R1050, Zymo Research). RT-qPCR was carried out using RevertAid First Strand cDNA synthesis kit (cat.K1622, Thermo Scientific) following manufacturer's protocol. PCR amplification was carried out using Brilliant III Ultra-Fast SYBR® Green qPCR mastermix (cat.600883, Agilent Technologies) and Agilent Mx3000P system. cDNA from *PTEN*$^{-/-}$ (PC3) and *PTEN* $^{+/+}$ (22Rv1) was used as fold-change control and Lamin A/C as housekeeping gene and internal control. Fold change (relative expression) was calculated using ddCT method. Primer pairs were designed to span exon-exon junctions, useful for limiting the amplification only to mRNA. The following sequences were utilized: PTEN: fwd 5′-ACCCACCACAGCTAGAACTT-3′, rev 5′-GGGAATAGTTACTCCCTTTTTGTC-3′; TNFRI: fwd 5′-CTGGAGCTGTTGGTGGGAAT-3′, rev 5′-TGACCCATTTCCTTTCGGCA-3′; Lamin A/C: fwd 5′-TGCAGGAGCTCAA TGATCGC-3′, rev 5′-CATTGTCAATCTCCACCAGTC-3′. In some experiments cell viability was measured using 3D CellTiter-Glo® 3D reagent (cat.G9681, Promega) by quantifying metabolically active cells releasing ATP. Cell line-derived organoids were plated at a density of 2000 cells per well in 96-well optical plates (cat.3610, Corning) embedded in Matrigel® as hanging drops (5 μL per well). Cells were treated with recombinant TNFα (cat 300-01A, PeproTech) at 10ng/ml and luminescence measurement was performed after 5 days in culture.

METHOD DETAILS

Necropsy and histopathology

Animals were necropsied and all tissues were examined regardless of their pathological status. Tumor size was measured by a tumor caliper and then applying the following formula: Size = (Width^2 × Length)/2. For the prostatic tumors, the size of two anterior lobes was considered. Normal and tumor tissue samples were fixed in 10% neutral-buffered formalin (Sigma) overnight. Tissues were processed by ethanol dehydration and embedded in paraffin according to standard protocols. Sections (5 μm) were prepared for antibody detection and hematoxylin and eosin (H&E) staining (Diapath, C0303) and (Diapath, C0363) respectively. To evaluate evidence of invasion, sections were cut at 20 μm intervals and H&E stained. Slides were prepared containing 3 to 5 of these interval sections. In all experiments the histology was evaluated blindly.

Immunohistochemistry and immunofluorescence

For immunohistochemistry (IHC), tissues were fixed in 10% formalin (Thermo Scientific, 5701) and embedded in paraffin in accordance with standard procedures. Preceding immunohistochemical staining, tumor sections were exposed to two washes with OTTIX plus solution (Diapath, X0076) and subsequent hydration with OTTIX shaper solution (Diapath, X0096) followed by deionized water. Antigen unmasking was performed by heating sections in the respective pH solutions based on the antibodies used at 98°C for 20 mins. Subsequently the sections were blocked for peroxidases and non-specific binding of antibodies using 3% H_2O_2 (VWR chemicals, 23615.248) and Protein-Block solution (DAKO Agilent technologies, X0909) respectively for 10 min each split by 0.5% PBST washing. Sections were stained for anti-p16 (M156; Santa Cruz), anti-Ki67 (Clone SP6; Lab Vision Corporation), anti-pH2AX and anti-CD31. Images were obtained using objectives of 5x and 20x magnification and Pixel image of 1.12 μm and 0.28 μm respectively. For the immunofluorescence (IF) staining, tissue paraffin embedded sections were stained

for anti-E-Cadherin (BD Biosciences, 610181), anti-Vimentin (Dako), anti-F4/80 (Serotec), anti-pHp1gamma (Cell signaling). Confocal images were obtained with the Leica TCS SP5 confocal microscope or Leica TCS SP8II. In all experiments the histology was evaluated blindly.

Prostatic epithelial cell purification and cytokine array

Pten$^{pc+/+}$, *Pten*$^{pc-/-}$ and *Pten*$^{pc-/-}$; *Trp53*$^{pc-/-}$ 12 weeks old mice were sacrificed and whole prostates were isolated and processed to single cell suspension for magnetic activated cells sorting (MACS). Single cells were stained with purified-anti-CD45 (leukocytes), and incubated 20 min on ice. Cells were then loaded into MS column (Miltenyi biotech) for MACS separation and unstained epithelial cells were collected in the negative fraction. Purified prostatic epithelial cell were processed as indicated in cytokine array kit (Proteome Profiler Mouse XL Cytokine Array, R&D Systems). Developed films were scanned and obtained images were analyzed using ImageJ 1.43u and background signals were subtracted from the experimental values. Experiments were performed in technical duplicate.

In vitro differentiation of Bone Marrow derived macrophages and Human THP-1-derived macrophages

Bone marrow derived macrophages (BMDMs) were differentiated *in vitro* as previously described (Fleetwood et al., 2009; Murray et al., 2014). Briefly, bone marrow precursors were flushed from long bones of C57BL/6N mice or CXCR2 KO mice and cultured in DMEM supplemented with 10% heat-inactivated-FCS media, in the presence of 10ng/ml of M-CSF or GM-CSF (Peprotech). At day 4 non-adherent cells were collected and cultured for a further 3 days in the presence of fresh media. On day 7, the media was replaced with complete media containing specific cytokines for macrophages polarization (pro-inflammatory phenotype: 10 ng/ml LPS and 10 ng/ml IFNγ; anti-inflammatory phenotype: 30 ng/ml IL-4, 30 ng/ml IL-13 and 100 ng/ml CXCL2). At day 10 cells were harvested and analyzed by flow cytometry and qRT-PCR. The human monocytic cell line THP-1 was treated for one day with PMA 100 ng/ml to obtain differentiated macrophages (Starr et al., 2018, Plos One). On the next day, cells were washed and media was replaced. For the production of the conditioned media, c.m. from human tumor cell line was added in presence or absence of αCXCR2 (1uM). After 48h cells were washed and media was replaced. After 48h c.m. from macrophages were collected and used to condition human tumor cell lines for 48h. Conditioned media from IFNγ/LPS and IL-4/IL-13 stimulated macrophages was used as control.

Western blot

Tissue and cell lysates were prepared with RIPA buffer (1x PBS, 1% Nonidet P40, 0.5% sodium deoxycholate, 0.1% SDS and protease inhibitor cocktail (Roche). Total protein concentration was measured using BCA Protein Assay Kit (Cat: 23225; Pierce, Rockford). Equal amounts of proteins were separated by SDS-PAGE and western blotted onto a 0.45 μm- nitrocellulose membrane. Membranes were blocked in 5% defatted milk in Tris-buffered saline containing 0.1% Tween-20 (TBST), probed with diluted antibodies and incubated at 4°C overnight. The following primary antibodies were utilized: rabbit polyclonal anti-Pten (1:1000 dilution, Cell Signaling), rabbit polyclonal anti-p16 (1:1000 dilution, clone M156; Santa Cruz Biotechnology), rabbit monoclonal anti-TNFR1 (1:1000 dilution, Cell Signaling), rabbit polyclonal anti-HSP90 (1:1000 dilution, Cell Signaling), mouse monoclonal anti-α-Tubulin (1:1000 dilution, Cell Signaling), rabbit monoclonal anti-STAT6 (1:1000 dilution, Cell Signaling), goat polyclonal anti-pSTAT6 (1:500 dilution, Santa Cruz Biotechnology). After washing in TBST, the membrane was incubated with secondary antibody conjugated with horseradish peroxidase (HRP) (dilution 1:5000, Cell Signaling). The protein bands were visualized using the ECL Western Blotting Substrate (Pierce).

Flow cytometry analysis

For phenotype analysis, isolated cells were re-suspended in PBS containing 1% FCS (Sigma-Aldrich) and were stained for 15 min at room temperature with anti–mouse monoclonal antibodies. Samples were acquired on a BD LSR-Fortessa flow cytometer (BD Biosciences) and a BD FACSymphony flow cytometer. When needed, cells were sorted from the prostate single-cell suspension using a FACSAria III cell sorter (BD Biosciences), after staining with specific antibodies for 30 min at 4°C in PBS containing 1% FCS. Data were analyzed using FlowJo software (TreeStar, Ashland, OR).

In vitro suppression assay

In vitro suppression assays were carried out in RPMI/10% FCS in 96-well U-bottom plates (Corning, NY). Either naive splenocytes, CD3+ cells isolated from murine lymph nodes or leucocytes isolated from murine peripheral blood were utilized to perform three different sets of suppression assays. In all sets of experiments isolated cells were labeled with 5 μM CFSE (Molecular Probes), and activated *in vitro* with anti-CD3 and anti-CD28 beads (Invitrogen) according to the manufacturer's instructions. Condition media of polarized macrophages was added to the culture. After 3-5 days, cells were acquired by BD LSR Fortessa or BD FACS Symphony and the proliferation of CFSE-labeled CD8$^+$ T cells was assessed upon staining with the following anti-mouse monoclonal antibodies: CD3 APC-Cy7 (clone B241616); CD4 PerCP-Cy5.5 (clone B240053); CD8 APC (clone 53-6.7). Analysis of the data was performed by FlowJo software.

Gene expression

Total RNA was quantified by NanoDrop ND-1000 Spectro-photometer (NanoDrop Technologies, Wilming-ton, DE) and RNA quality was assessed using Agilent 2100 bioanalyzer (Agilent Technologies, Santa Clara, CA). Gene expression profiling was carried out using the one-color labeling method: labeling, hybridization, washing, and slide scanning were performed following the manufacturers protocols (Agilent Technologies). Briefly, 100 ng of total RNA were amplified, labeled with Cy3-CTP and purified with columns. Six-hundred ng of labeled specimens were hybridized on Agilent SurePrint G3 Mouse 8x60K Gene Expression arrays. After 17 h the slide was washed and scanned using the Agilent Scanner version C (G2505C, Agilent Technologies). Raw data were processed using the Bioconductor package Limma (Linear models for microarray analysis). Background correction was performed with the *normexp* method with an offset of 50, and *quantile* was used for the between-array normalization. The empirical Bayes method was used to compute a moderated t-statistics in order to identify differentially expressed genes in treated versus not treated mice. Data analysis and data visualization for the underlying GS-GS network and the superimposed GS-cluster network were carried out following the methodologies previously described(Delaleu et al., 2013). Parameters deviating from the original description are: i) GS collection updated to May 1st 2017, ii) gene ranking for GSEA based on fold change (genes 44064; n = 3 per group, Agilent SurePrint G3 Mouse GE 8x60K microarray), iii) Significance threshold for GSs being mapped: FDRq < 0.001 and TAGS $\geq$ 50, iv) layout algorithm: Cytoscape 3.5.0, yFiles organic layout 2 with edge connectivity threshold 0.065, v) inflation parameter for MCL clustering: 2.0 and vi). Cluster label annotation was supported by Auto Annotate(Su et al., 2014).

Real-time PCR

RNA was isolated by TRIzol reagent (QIAGEN) and retro-transcribed using SuperScriptIII (Invitrogen, 11752-250) according to the manufacturer's instructions. Quantitative PCR (RT-qPCR) reactions (Bio-Rad) for each sample were done in triplicate using KAPA SYBR FAST qPCR green (KK4605) (Applied Biosystems). The primer sequences were obtained from PrimerBank (http://pga.mgh.harvard.edu/primerbank/index.html). Each value was adjusted by GADPH level as reference.

Screening of macrophage-derived factors

Pten$^{+/+}$; *Trp53*$^{+/+}$ and *Pten*$^{-/-}$; *Trp53*$^{-/-}$ MEFs were plated at a density of 5 × 10^3 cells /ml. Both female and male derived MEFs were utilized. 2h after the cell plating, the following recombinant proteins were added to the cells as a single agent or in combination with another cytokine/chemokine: 100 ng/ml IL6, 100 ng/ml CXCL5, 100 ng/ml IL-1α, 10 ng/ml TNFα, 10 ng/ml GM-CSF, 100 ng/ml IL-12, 200 ng/ml CCL5, 250 ng/ml adiponectin. Recombinant cytokines were purchased from Peprotech. At day 3 the cell viability was tested by crystal violet staining proliferation assay. Briefly, conditional media was aspirated and the cells were gently washed twice with PBS. The cell fixation was performed by adding 10% Formalin for 10 min. The cells were gently washed with PBS and stained with 0.05% Crystal Violet for 20 min. After the staining, crystal violet was discarded; the cells were washed in water and dried at room temperature overnight. Absorbance was read using the Microplate Reader at 590 nm.

Co-culture of MEFs with murine macrophages conditioned media

In the co-culture experiments, conditioned media from either IFNγ/LPS or IL-4/IL-13 polarized macrophages was added to the MEFs 1 day after seeding. Co-cultures were stopped 72hrs later and cells harvested for protein extraction or stained for analysis. Senescence was assessed by mean of a Senescence β-Galactosidase Staining Kit (Cell Signaling, 9860).

Phagocytosis assay

Briefly, murine bone marrow derived macrophages were exposed to the conditioned media collected from TRAMP-C1 prostate cancer cells, to recapitulate the effect of cancer cells on infiltrating macrophages. Tumor-conditioned macrophages were co-coltured with RFP-labeled TRAMP-C1 cancer cells overnight, in presence or absence of αCXCR2 to assess the phagocytic activity versus tumor cells. Cells were then collected and analyzed by flow cytometry following staining for macrophage markers with the following anti-mouse monoclonal antibodies: CD11b APC (clone M1/70); F4/80 eFluor780 (clone BM8). The frequency of RFP$^+$ F480$^+$ cells was quantified to assess the phagocytic activity of macrophages.

QUANTIFICATION AND STATISTICAL ANALYSIS

Statistical analyses were performed using a two-tailed unpaired Student's t test. Values are presented as mean ± SEM (*p < 0.05; **p < 0.01; ***p < 0.001). For studies comparing more than two groups, 2-way ANOVA multiple comparisons by Prism6 was also utilized. Differences were considered significant when *p < 0.05 or are indicated as not significant (ns).

DATA AND CODE AVAILABILITY

The accession number for the RNA-sequencing dataset reported in this paper is GEO: GSE125273.

Cell Reports, Volume *28*

Supplemental Information

Re-education of Tumor-Associated Macrophages by CXCR2 Blockade Drives Senescence and Tumor Inhibition in Advanced Prostate Cancer

Diletta Di Mitri, Michela Mirenda, Jelena Vasilevska, Arianna Calcinotto, Nicolas Delaleu, Ajinkya Revandkar, Veronica Gil, Gunther Boysen, Marco Losa, Simone Mosole, Emiliano Pasquini, Rocco D'Antuono, Michela Masetti, Elena Zagato, Giovanna Chiorino, Paola Ostano, Andrea Rinaldi, Letizia Gnetti, Mariona Graupera, Ana Raquel Martins Figueiredo Fonseca, Ricardo Pereira Mestre, David Waugh, Simon Barry, Johann De Bono, and Andrea Alimonti

Supplementary Figure 1

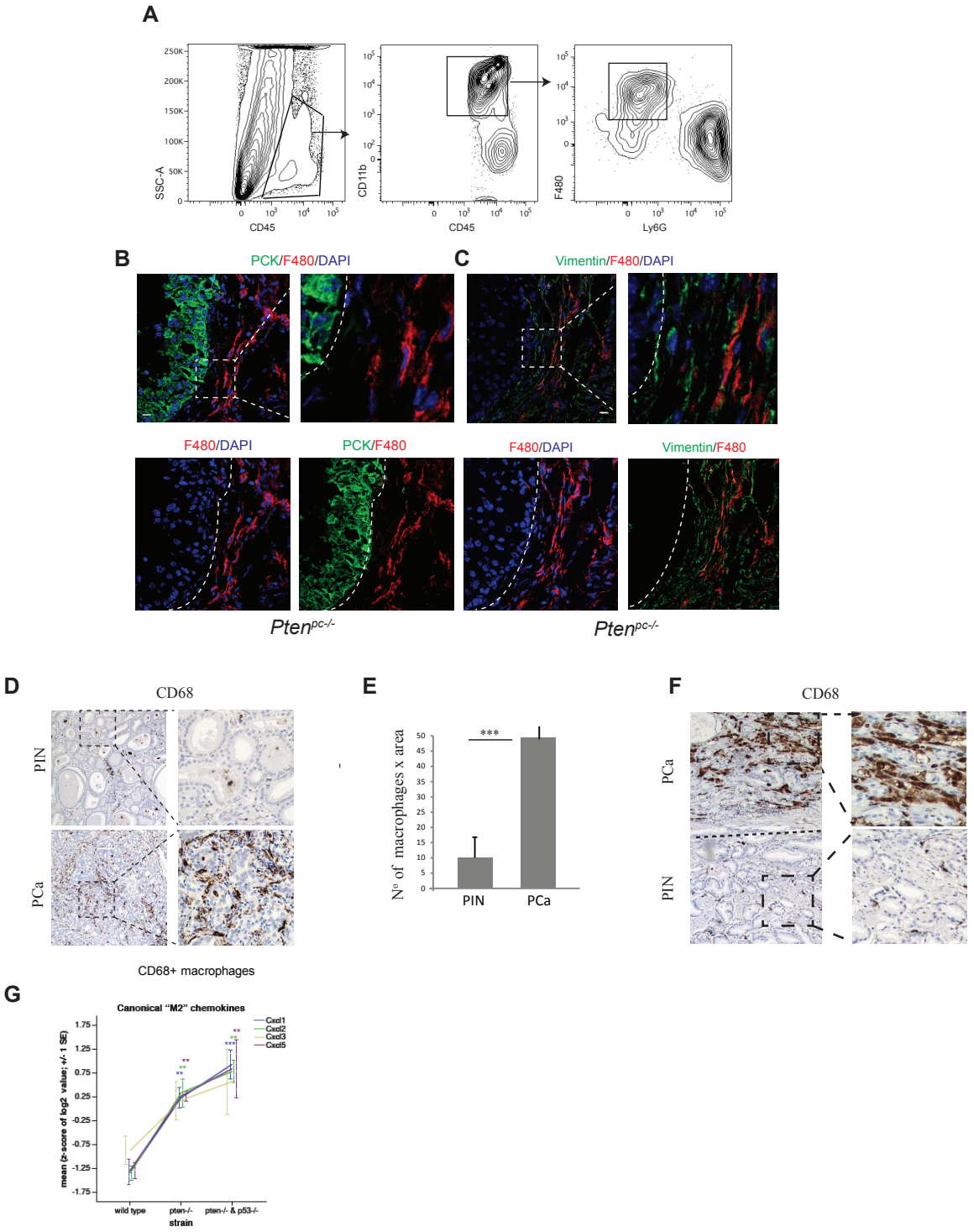

Supplementary Figure 1. TAMs infiltration correlates with tumor progression in murine and human prostatic tumors. Related to Figure 1.

(A) Representative FACS plots of the gating strategy utilized for the characterization and quantification of CD45+CD11b+F480+ TAMs in *Pten*$^{pc-/-}$ and *Pten*$^{pc-/-}$; *Trp53*$^{pc-/-}$ tumors. (B) Representative confocal immunofluorescence images (IF) showing the localization of F4/80^{+} (red) macrophages in *Pten*$^{pc-/-}$ prostatic tumors. Prostatic epithelial tissues are stained with αPan-Cytokeratin (PCK, green). Cells were counterstained with the nuclear marker DAPI (blue). Scale bar: 10 μm (C) Representative confocal immunofluorescence images of F4/80^{+} (red) tumor-infiltrating macrophages and vimentin^{+} cells (green) within anterior prostate lobes from *Pten*$^{pc-/-}$ tumors. Cells were counterstained with the nuclear marker DAPI (blue). Scale bar: 10μm. (D) Representative images and (E) quantification of CD68 IHC staining in adjacent areas of a prostatic tumor, showing TAMs infiltrating in PIN vs PCa areas. Analyses were performed on a human Tissue Microarray (TMA) including N= 10 PIN e N=11 PCa cases. Original magnification 20X. (F) Representative image of a TMA section where PIN and PCa areas co-existed. CD68 staining shows here the preferential infiltration of macrophages in PCa areas. Original magnification 20X. (G) Gene expression levels of CXCL chemokines in tumor tissues from *Pten*$^{pc+/+}$, *Pten*$^{pc-/-}$ and *Pten*$^{pc-/-}$; *Trp53*$^{pc-/-}$ mice, obtained from wild-type mice and prostate cancer models (GSE25140(Ding et al., 2011); probe with highest signal per gene). Group means were compared by computing 1-way Anova with Dunnett's as post-test (SPSS v. 23). Wild-type served as the reference and p-values two-tailed < 0.05 were considered significant. * P<0.05, ** P<0.01, ***P<0.001.

Supplementary Figure 2

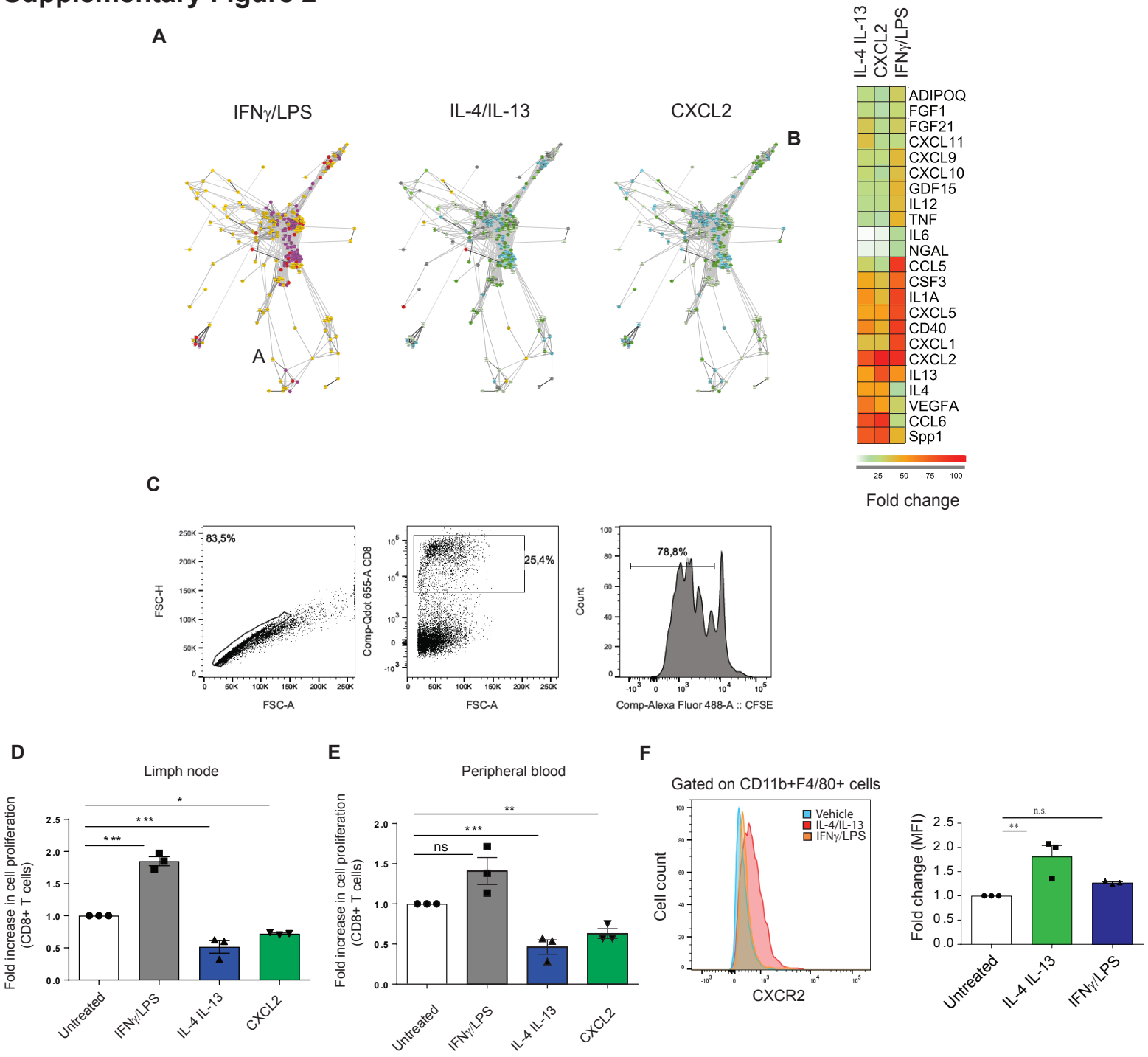

Supplementary Figure 2. Role of the CXCL2-CXCR2 pathway on macrophage polarization *in vitro*. Related to Figure 2. (A) Identification of all gene sets (GSs) pivotal in macrophage polarization with IL-4/IL-13 and IFNγ/LPS from bone marrow-derived macrophage in vitro and their behavior in context with CXCL2-mediated differentiation. Gene set (GSs) enrichment analyses were run on the respective lists (IL-4/IL-13 versus Untreated, CXCL2 versus Untreated and IFNγ/LPS versus Untreated), collapsed for probes yielding the highest signal per gene and ranked for fold-change. 23304 GSs were subjected to analyses of which 8556 were interrogated after filtering for GS-size. GSs enriched in IFNγ/LPS versus untreated and at the same time depleted when comparing IL-4/IL-13 versus untreated or vice versa formed the basic GS-network of pivotal pathways. Network organization is representative of the degree of GS-members connected GSs share (threshold for solid edges ≧ 5%, Cytoscape 3.1.1). For each comparison each node's color denotes significant enrichment (orange = FDRq < 0.05; red = FDRq < 0.01; purple = FDRq < 0.001) or significant depletion (light green = FDRq < 0.05; green = FDRq < 0.01; cyan = FDRq < 0.001) of this GSs. Comparing the three networks, the transcriptional landscape of CXCL2-stimulated macrophages corresponded to 83.6% with IL-4/IL-13 and to 3.8% with IFNγ/LPS. 12.7% of the GSs pivotal to IFNγ/LPS-IL-4/IL-13 differentiation were unaltered following CXCL2 stimulation (node color = grey). (B) Cytokine protein profile of macrophages exposed to IFNγ/LPS, IL-4/IL-13 and CXCL2. Protein profiling was obtained through a cytokine array quantifying 110 proteins (see Methods). Experiment was performed in technical duplicates. (C) Representative FACS plot of the gating strategy utilized for the T cells suppression assay. We analyzed the frequency of CFSE negative (proliferating) cells among $CD8^+$ T lymphocytes. (D,E) Bar graphs showing the quantification of CFSE proliferation assay performed on T cells from (D) Lymph nodes and (E) peripheral blood exposed to macrophages-derived conditioned media in presence or absence of aCXCR2. CSFE negative (proliferating) cells were gated among $CD3^+CD8^+$ cells. (n=3). (F) FACS plot (left panel) and quantification (right panel) showing the frequency of $CXCR2^+$ macrophages upon stimulation with IFNγ/LPS and IL-4/IL-13 in vitro. Mean fluorescence intensity has been measured in CD11b+F480+cells. * P<0.05, ** P<0.01, ***P<0.001.

Supplementary Figure 3

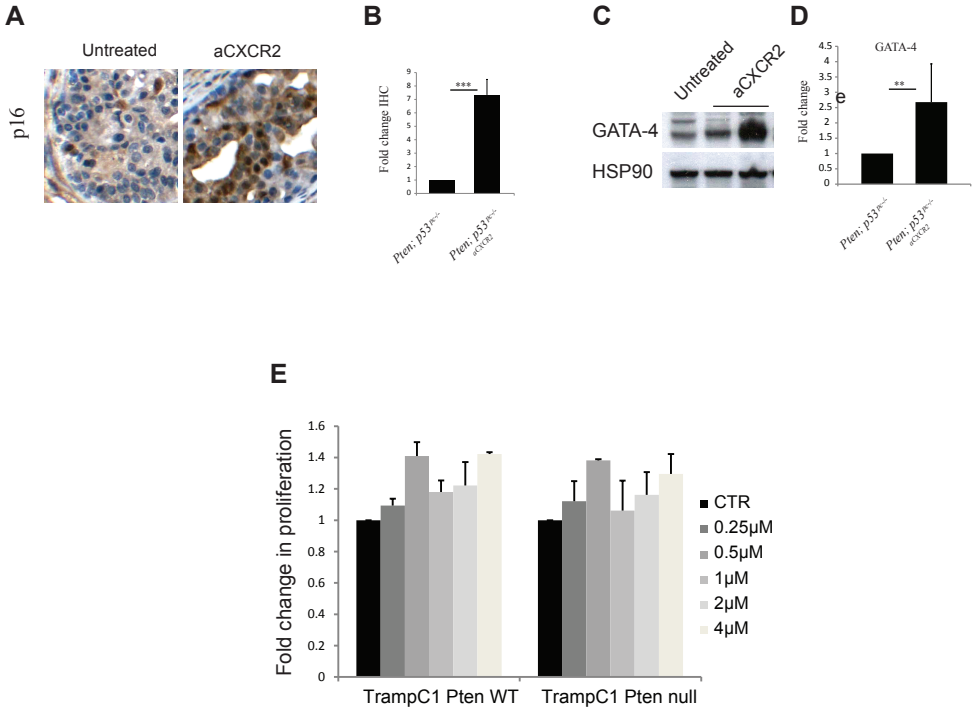

Supplementary Figure 3. TAMs are reprogrammed toward a pro-inflammatory functional state upon treatment with αCXCR2 *in vivo*. Related to Figure 3.

(A) Representative IHC staining (original magnification 20X) and (B) quantification of p16 expression in *Pten*$^{pc-/-}$; *Trp53*$^{pc-/-}$ prostatic tumors upon treatment with αCXCR2 (insert). (C) Western blot analysis and (D) quantification of GATA-4 expression in tumors of mice with or without αCXCR2 treatment. (E) Bar graph showing fold change in proliferation of TRAMP-C1 prostate cancer cells upon exposure to αCXCR2 at different dosages. Cell proliferation was assessed using crystal violet staining. ***P<0.001.

Supplementary Figure 4

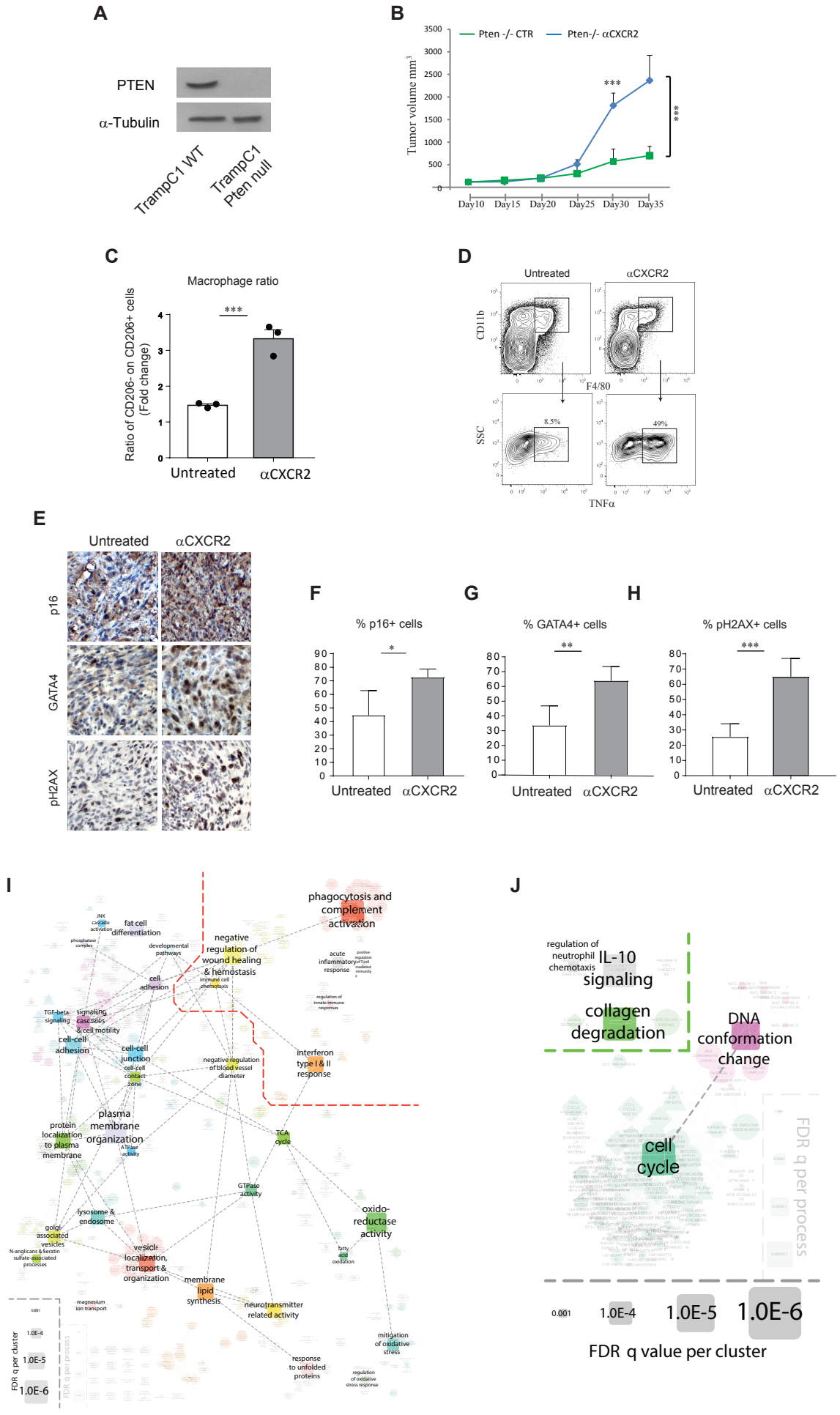

Supplementary Figure 4. αCXCR2 administration reprograms TAMs leading to tumor inhibition in a murine allograft model. Related to Figure 3. (A) Western blot analysis showing *Pten* expression in TRAMP-C1 cells before and after CRISPR/Cas9 mediated deletion. CRISPR/Cas9 was performed on TRAMP-C1 cells to delete *Pten*. (B) Graphs showing the tumor volume of TRAMPC1-*Pten*$^{-/-}$ cells injected subcutaneously, in presence or absence of αCXCR2 treatment. (C) Bar graph from FACS analysis showing the fold change in the ratio between $CD45^{+}CD11b^{+}F4/80^{+}CD11c^{+}CD206^{-}$ and $CD45^{+}CD11b^{+}F4/80^{+}CD11c^{+/-}CD206^{+}$ macrophages infiltrating the TRAMP-C1 allografts. (D) Representative FACS plots of the intracellular staining of TNFα secreted by $CD11b^{+}F4/80^{+}$ tumor infiltrating macrophages upon αCXCR2 treatment. Events are gated on $CD45^{+}$ cells. (E) Representative images of IHC stainings and quantification of (F) p16, (G) GATA4 and (H) pH2AX in TRAMPC1 Pten-/-; Trp53-/- allografts, in presence or absence of the αCXCR2 treatment. Original magnification 20X. (I) Gene set (GS)-cluster network superimposed on the original transcriptional landscape that maps all GSs significantly enriched in FACS sorted TAMs ($CD45^{+}F480^{+}$ cells) after treatment of the tumor bearing mice with the CXCR2 antagonist. The area outlined by the red boarder comprises the significantly upregulated immunity-associated effector processes. For the GS-cluster network superimposed on the GS-GS network: Node color = MCL-cluster; node size = inversely proportional to mean log2 transformed FDRq values of the GSs belonging to this cluster. For the GS-GS network in the background: Node color = MCL-cluster membership; node size = inversely proportional to log2 transformed FDRq values, node shape = database resource; edge color = darker the higher the proportion of leading edge genes overlapping between the nodes it connects is. Data analysis and data visualization for the underlying GS-GS network and the superimposed GS-cluster network were carried out following the methodologies described in detail in the Methods. (J) The area outlined by the green boarder comprises the significantly downregulated immunity-associated effector processes. Underlying analyses, visualization methodology and layout parameters of panel J correspond precisely to the ones listed for panel I. The FDR*q* value reference nodes allow estimation of scaling and direct comparison of the two panels (n=4 samples/group). * $P<0.05$, ** $P<0.01$, *** $P<0.001$.

Supplementary Figure 5

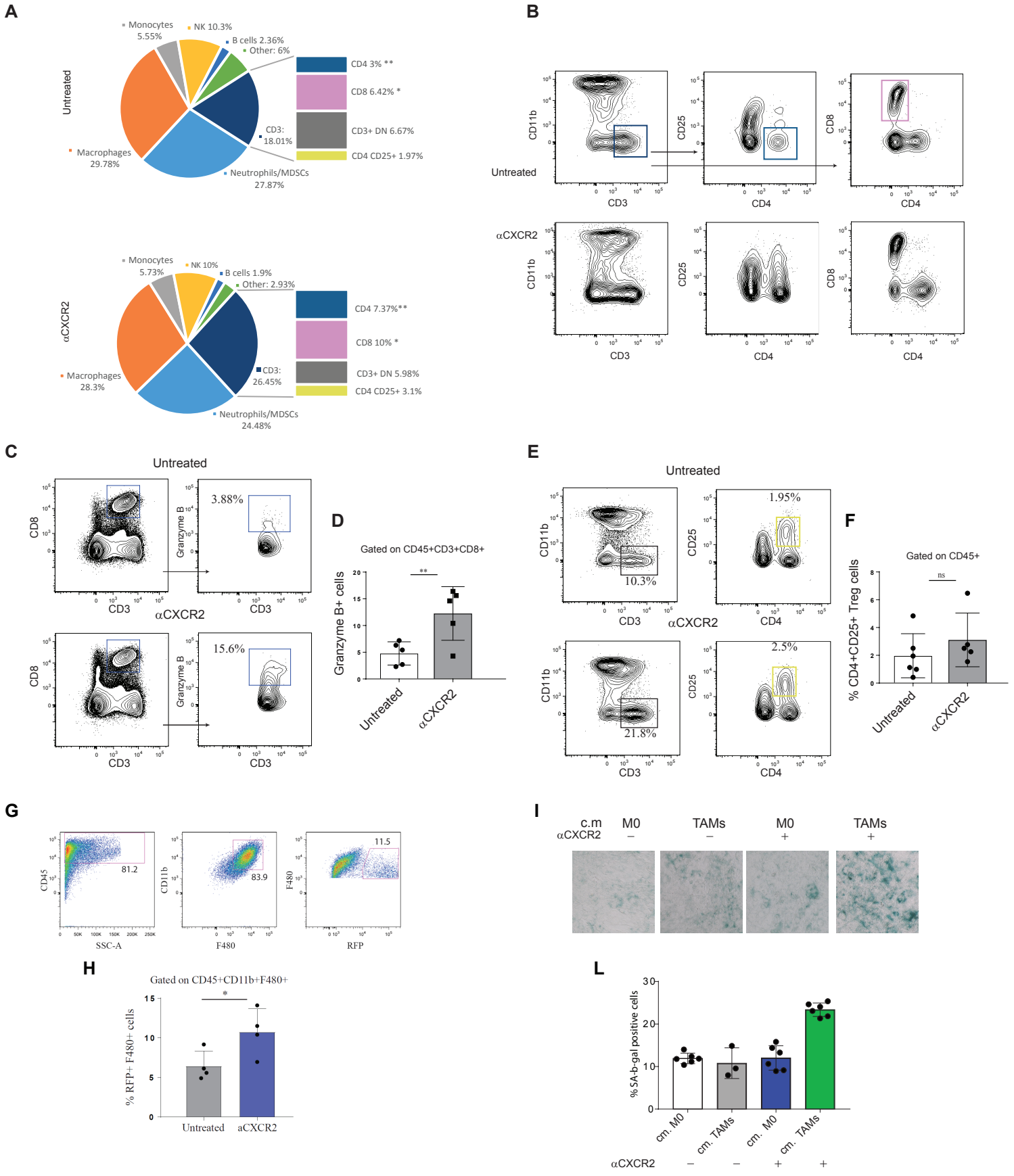

Supplementary Figure 5. ***In vivo*** **αCXCR2 effect on the immune cells infiltrate. Related to Figure 3.**

(A) Pie charts showing percentages of tumor infiltrating immune cells with or without αCXCR2 treatment. Vertical slices on the right of each pie chart represents the different $CD3^+$ subpopulations. Events were gated on $CD45^+$ cells. (n= 5 mice per group) (B) Gating strategy utilized to define $CD4^+$ and $CD8^+$ cells in the untreated (upper panel) and in the αCXCR2 treated mice (lower panel). (C) Representative FACS plots and (D) bar graph showing the percentage of $CD8^+$ Granzyme B^+ T cells that infiltrate the tumor upon aCXCR2 treatment, compared to the untreated tumors. (E) Representative FACS plots and bar graph (F) showing the percentage of $CD4^+$ $CD25^{high}$ T regulatory cells that infiltrate the tumor upon aCXCR2 treatment, compared to the untreated tumors. (G) Representative FACS plots and (H) bar graph showing the percentage of RFP^+ phagocytic macrophages. Events are gated on $CD45^+CD11b^+F4/80^+$cells. (I) Representative images and (J) bar graph showing the quantification of SA-β-galactosidase positive TRAMP-C1 cells exposed to c.m. from macrophages polarized *in vitro* with c.m. from *Pten* $^{-/-}$;Trp53 $^{-/-}$ cells ± αCXCR2. ***P<0.001**, P<0.01, *P<0.05.

Supplementary Figure 6

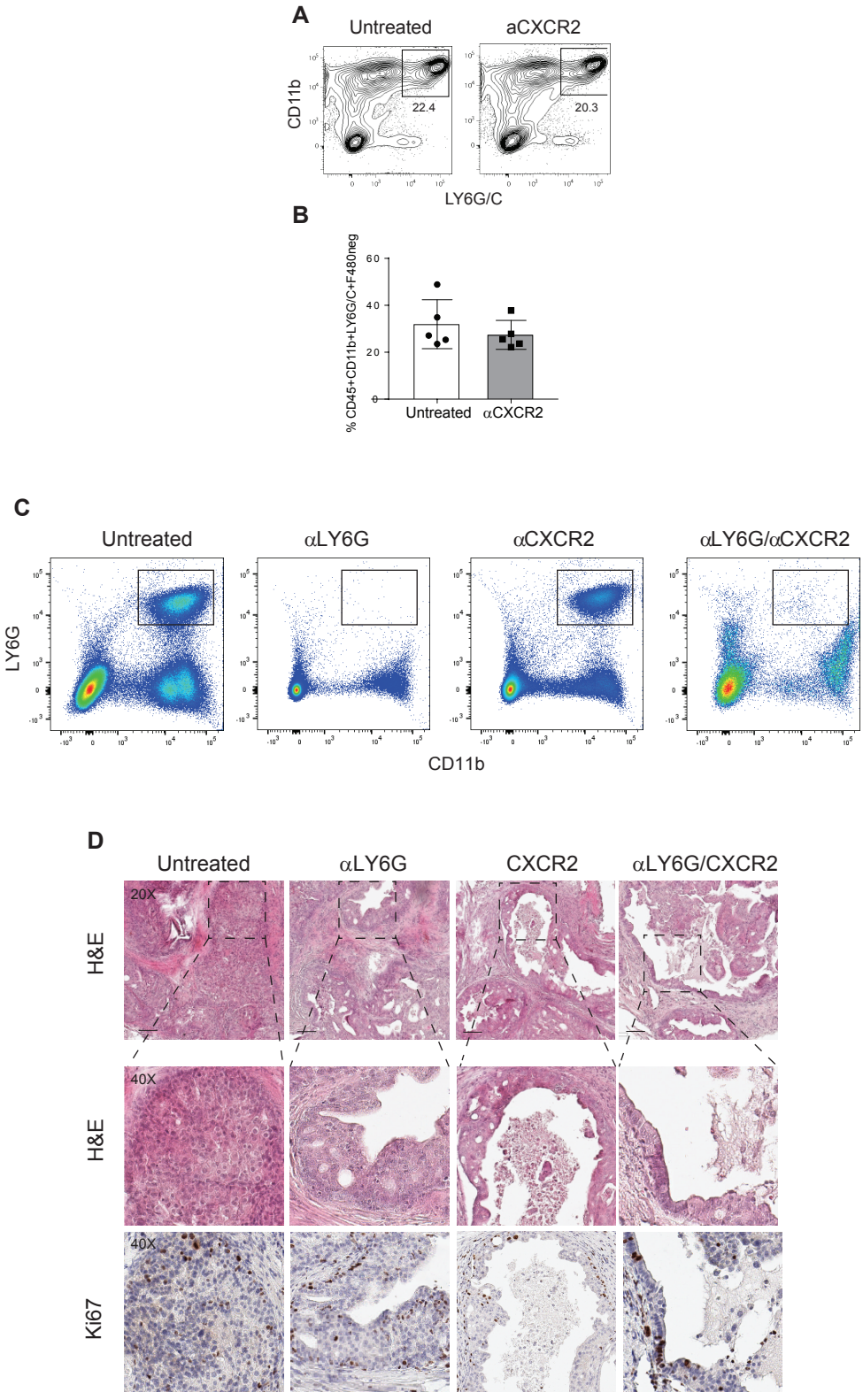

Supplementary Figure 6. ***In vivo*** **αCXCR2 effect on TAMs re-education and tumor inhibition is not affected by Ly6G^{+} cells depletion. Related to Figure 3.**

(A) Representative FACS plots and (B) quantification of the frequency of CD11b^{+} Ly6G/C^{+} tumor infiltrating cells with or without αCXCR2 treatment in *Pten*$^{pc-/-}$; *Trp53*$^{pc-/-}$ mice. Events are gated on CD45^{+} cells. (n=5 mice per group). (C) Representative FACS plots of the frequency of CD11b^{+}Ly6G^{+} circulating cells in peripheral blood and (D) representative images of hematoxylin and eosin (H&E) and Ki67 IHC tumor staining in *Pten*$^{pc-/-}$; *Trp53*$^{pc-/-}$ mice upon daily treatment with 1A8(αLy6G), αCXCR2 or 1A8(αLy6G)/αCXCR2, for 3 weeks. Original magnification 20X. Scalebar: 100μM

Supplementary Figure 7

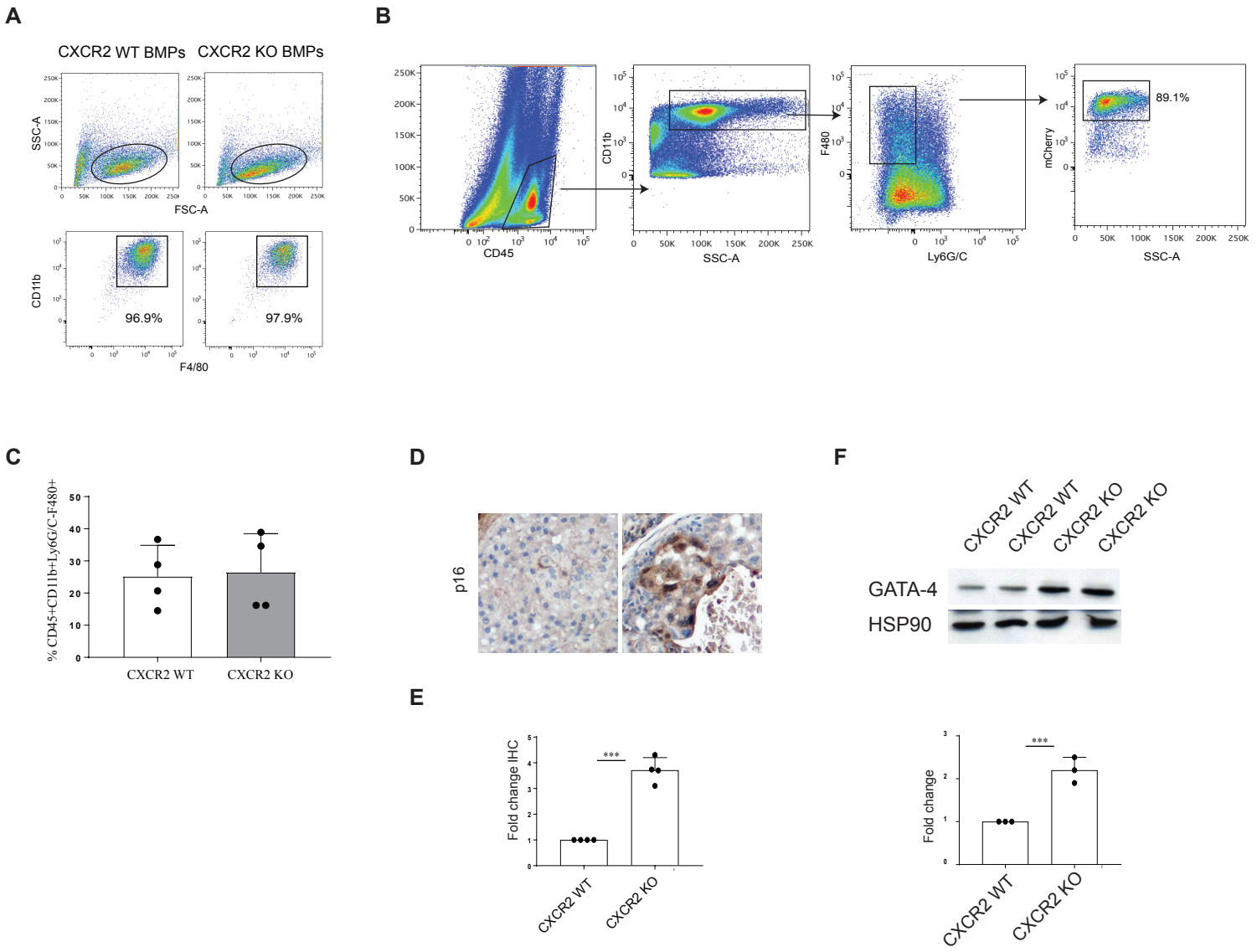

Supplementary Figure 7. Infusion of CXCR2 KO monocytes (vs CXCR2 WT monocytes) in *Pten*$^{pc-/-}$; *Trp53*$^{pc-/-}$ mice drives tumor inhibition and senescence induction. Related to Figure 4.

(A) Representative FACS plots of the gating strategy utilized for the characterization of CXCR2 WT and CXCR2 KO BMDMs after 7 days of *in vitro* differentiation. (B) Representative FACS plots of the gating strategy showing the infiltration of CXCR2 KO UBC-mCherry-labelled monocytes in the tumor after infusion in *Pten*$^{pc-/-}$; *p53*$^{pc-/-}$ mice. *Pten*$^{pc-/-}$; *p53*$^{pc-/-}$ mice were infused with CXCR2 WT or CXCR2 KO monocytes as described in the methods. (C) Bar graph showing the frequency of F4/80^{+} macrophages in tumors of mice infused with CXCR2 WT and CXCR2 KO monocytes. Events are gated in CD45^{+}CD11b^{+} cells. (n= 4 mice per group) (D) Representative images of IHC staining (original magnification 40X) and (E) quantification of western blot analysis of p16 expression in mice upon CXCR2 WT and CXCR2 KO monocytes infusion. (F) Western blot analysis (upper panel) and quantification (lower panel) of GATA-4 expression in tumors after infusion with CXCR2 WT and CXCR2 KO monocytes. ***P<0.001.

Supplementary Figure 8

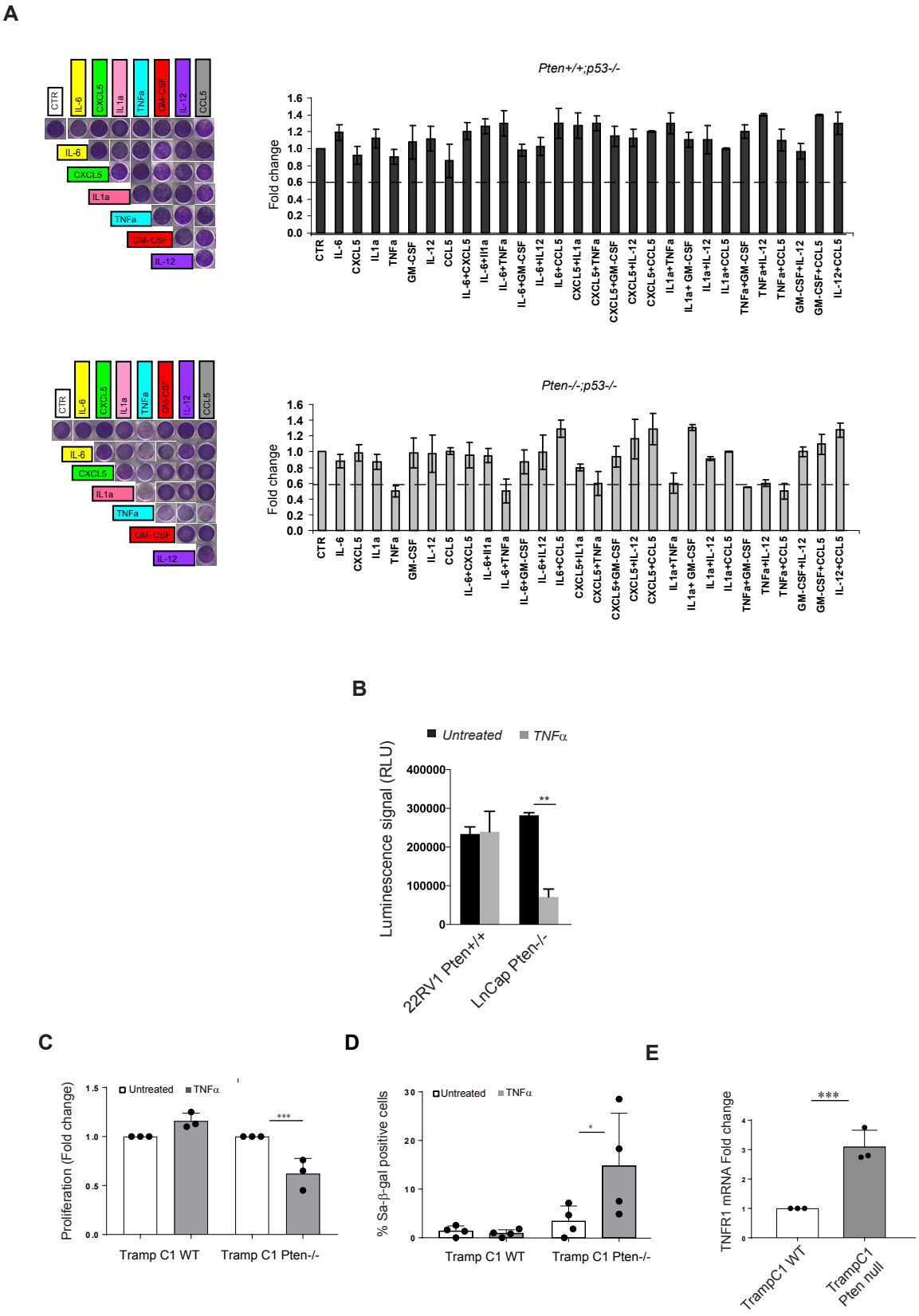

Supplementary Figure 8. *Pten* deletion sensitizes MEFs to TNFα-induced stop of proliferation. Related to Figure 5.

(A) Representative pictures and bar graphs showing the fold change in proliferation of Pten$^{+/+}$; p53$^{-/-}$ (upper panel) and Pten$^{-/-}$, p53$^{-/-}$ MEFs (lower panel) upon exposure to different combinations of cytokines. (B) *In vitro* treatment of 22Rv1 and LNCap cell lines-derived organoids with recombinant TNFα (10 ng/ml). Proliferation was measured by luminescence signal (RLU) after 5 days (C) Bar graph showing the fold change in proliferation of TRAMPC1 Pten$^{+/+}$ and Pten$^{-/-}$ cells exposed to TNFα (10 ng/ml) for 3 days (n=4). (D) Bar graph showing the quantification of SA-β-gal staining on TRAMP-C1 Pten$^{+/+}$ and Pten$^{-/-}$ cells exposed to TNFα for 3 days (n=4). (E) qRT-PCR analysis of *TNFR1* expression in *Pten*$^{+/+}$ and *Pten*$^{-/-}$ TRAMP-C1 cell line (n=3). * P<0.05, ***P<0.001.